FABRICATION AND CHARACTERIZATION OF NANO-SIZED MAGNETIC STRUCTURES AND THEIR FLUX-PINNING EFFECTS ON SUPERCONDUCTING THIN FILMS

A Dissertation

by

HAN GIL LEE

Submitted to the Office of Graduate Studies of
Texas A&M University
in partial fulfillment of the requirements for the degree of

DOCTOR OF PHILOSOPHY

December 2010

Major Subject: Applied Physics

Fabrication and Characterization of Nano-Sized Magnetic Structures and Their Flux-Pinning Effects on Superconducting Thin Films

FABRICATION AND CHARACTERIZATION OF NANO-SIZED MAGNETIC STRUCTURES AND THEIR FLUX-PINNING EFFECTS ON SUPERCONDUCTING THIN FILMS

A Dissertation

by

HAN GIL LEE

Submitted to the Office of Graduate Studies of
Texas A&M University
in partial fulfillment of the requirements for the degree of

DOCTOR OF PHILOSOPHY

Approved by:

Chair of Committee,	Donald G. Naugle
Committee Members,	Igor Lyuksyutov
	Winfried Teizer
	Hong Liang
Head of Department,	Edward Fry

December 2010

Major Subject: Applied Physics

ABSTRACT

Fabrication and Characterization of Nano-Sized Magnetic Structures and Their Flux-Pinning Effects on Superconducting Thin Films. (December 2010)

Han Lee, B.S.,Yonsei University; M.S., Yonsei University;

M.S., Texas A&M University

Chair of Advisory Committee: Dr. Donald G. Naugle

This dissertation describes experimental studies of how a spatially alternating magnetic field can effectively pin the magnetic flux in a superconducting thin film ($Pb_{82}Bi_{18}$), thereby enhancing the superconductivity. The spatially alternating magnetic field was provided by a periodic array of nano-sized magnetic structures: 300 nm spacing triangular array of cobalt rods with 100 nm diameter and 300 nm height. The superconducting film deposited on top of the magnetic structures, or an embedded Ferromagnet- Superconductor Hybrids (FSH), showed enhanced critical current and critical magnetic field. The embedded FSH also showed the field matching effect, the field compensation effect, and hysteresis.

This dissertation also explains how to fabricate and characterize magnetic nano-structures. Electron beam lithography and electroplating method were used to fabricate the magnetic nanostructures. Scanning electron microscopy (SEM) and atomic force microscopy (AFM) were used to characterize the structures of the magnetic rods. Magnetic force microscopy (MFM) was used to study their magnetic properties.

ACKNOWLEDGEMENTS

My sincere thanks go to my committee chair, Dr.Naugle, for his invaluable assistance and advice toward completing this work. I consider my association with him throughout my research a distinct privilege.

Special recognition goes to my wife, Jin Hee Kim, who has been a constant source of encouragement throughout my life.

TABLE OF CONTENTS

CHAPTER Page

LIST OF FIGURES

FIGURE Page

FIGURE Page

FIGURE Page

CHAPTER I

INTRODUCTION

Brief Review of Superconductors

Depending on the behavior of superconductors in magnetic fields, superconductors fall into two categories: type I superconductor and type II superconductor.

Type I Superconductors

If an external field $\boldsymbol{H}$ is smaller than a critical field $\boldsymbol{H}_c\ (T)$, the type I superconductor completely expels the magnetic flux from its interior (Meissner effect);

$$B = H\ + 4\pi M = 0,$$

where B is the magnetic flux density and M is the sample magnetization .

As the external magnetic field increases above the critical field $\boldsymbol{H}_c\ (T)$, the superconductor returns to the normal conducting state (Fig.1).

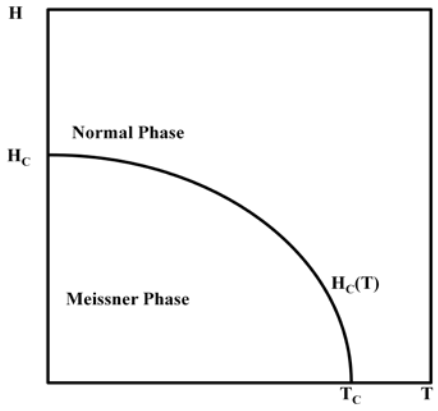

Fig.1. Phase diagram of a Type I superconductor.

This dissertation follows the style of Journal of Magnetism and Magnetic Materials.

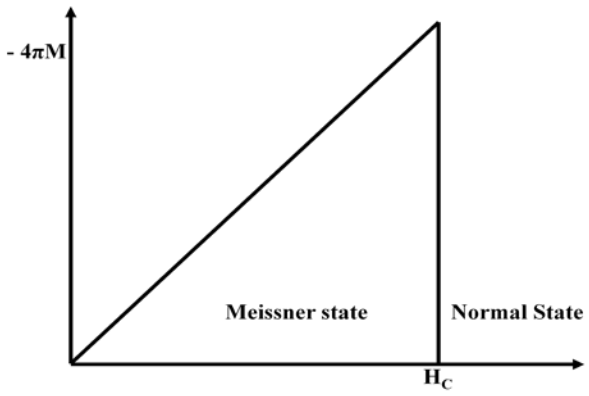

Fig. 2. The field dependence of the magnetization of a bulk Type I superconductor.

The magnetization M versus the applied magnetic field H is shown in Fig.2. Below the critical field the type I superconducting material becomes a perfect diamagnetic material. However, depending on the shape or the demagnetization factor of a type I superconductor, magnetic flux penetrates in the form of continuous lamina (Fig. 3). A superconductor in such a state is said to be in the intermediate state [1, 2].

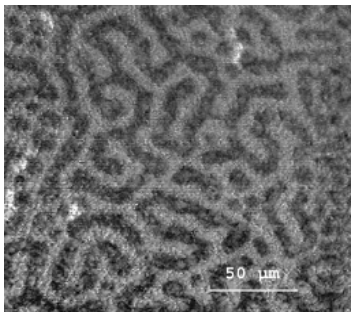

Fig.3. Meandering laminar structure with alternating domains of normal and superconducting regions with the magnetic field normal to the superconductor film. The high resolution magneto-optical imaging technique was used to characterize the structure [3].

Type II Superconductors

If an external field $\boldsymbol{H}$ is smaller than a critical field $\boldsymbol{H}_{c1}\ (T)$, the magnetic response of the type II superconductor is the same as that of the type I superconductors (Meissner effect). However, as the external magnetic field increases above the lower critical field and below an upper critical field $\boldsymbol{H}_{c2}\ (T)$, the magnetic flux partially penetrates the sample in the form of tubes, or vortices (Fig.4). This state is said to be a vortex state or mixed state [1, 2].

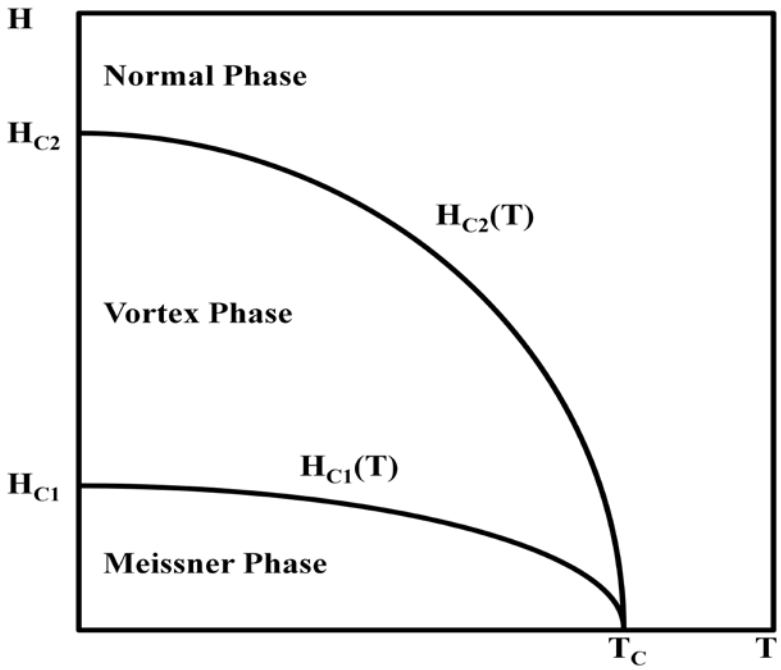

Fig. 4. Phase diagram of a Type II superconductor.

Fig.5 shows the magnetization versus the applied magnetic field :below H_{c1}, the specimen in the superconducting state shows ideal diamagnetic behavior like in a Type I superconductor ;but for $H_{c1} < H < H_{c2}$, unlike a sudden transition in a Type I superconductor (Fig.2), the magnetization decreases in a continuous way in the vortex state, as the applied magnetic field increases ;and above the second critical field H_{c2} , the specimen becomes a normal conducting state.

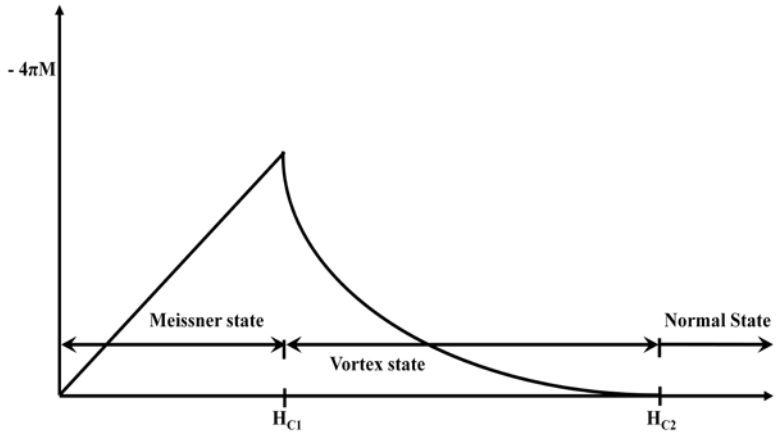

Fig.5. Magnetization versus applied field H for a type II superconductor.

In the vortex state, type II superconductors allow magnetic fields to penetrate in the form of vortices. Each vortex consists of a core of normal metal where the superconductivity is destroyed by the magnetic field and which is surrounded by a circulating supercurrent. Also, each vortex carries a quantum magnetic flux equal to

$$\Phi_0 = \frac{hc}{2e} = 2.0678 \times 10^{-7} \text{ gauss} \cdot cm^2.$$

This unit of flux is called a fluxoid or fluxon.

Fig.6 shows a model of a vortex as a core of normal metal allowing the fluxoid Φ_0. The cylindrical core has a radius of ξ, the coherence length. The coherence length represents the width of the region over which the density of the superconducting charge carriers changes from zero at the center of the core (normal conductor) to that of the bulk superconductor at the core radius. The magnetic field and screening current fall off over a distance of λ, the penetration depth.

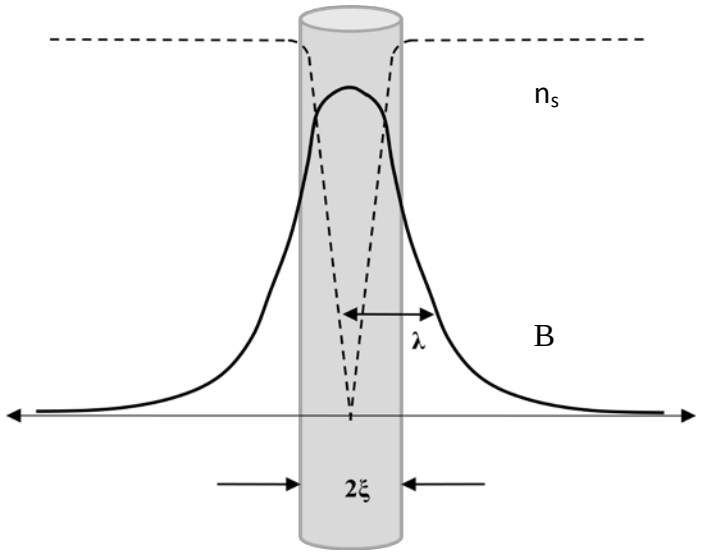

Fig. 6. Model of a vortex. The order parameter, or the density of superconducting electrons falls to zero at the center of the vortex [1, 2].

From the penetration depth and coherence length, the two critical fields can be estimated [1, 2]:

$$\boldsymbol{H}_{c1} \approx \frac{\Phi_0}{\pi\lambda^2}$$

$$\boldsymbol{H}_{c2} \approx \frac{\Phi_0}{2\pi\xi^2.}$$

Depending on the ratio $\kappa = \frac{\lambda}{\xi}$ of a superconductor, the superconductor can be either type I or type II :

$$\kappa = \frac{\lambda}{\xi} < \frac{1}{\sqrt{2}} \qquad \text{type I}$$

$$\kappa = \frac{\lambda}{\xi} > \frac{1}{\sqrt{2}} \qquad \text{type II.}$$

Fig. 7 shows the length scales in type I and type II superconductors.

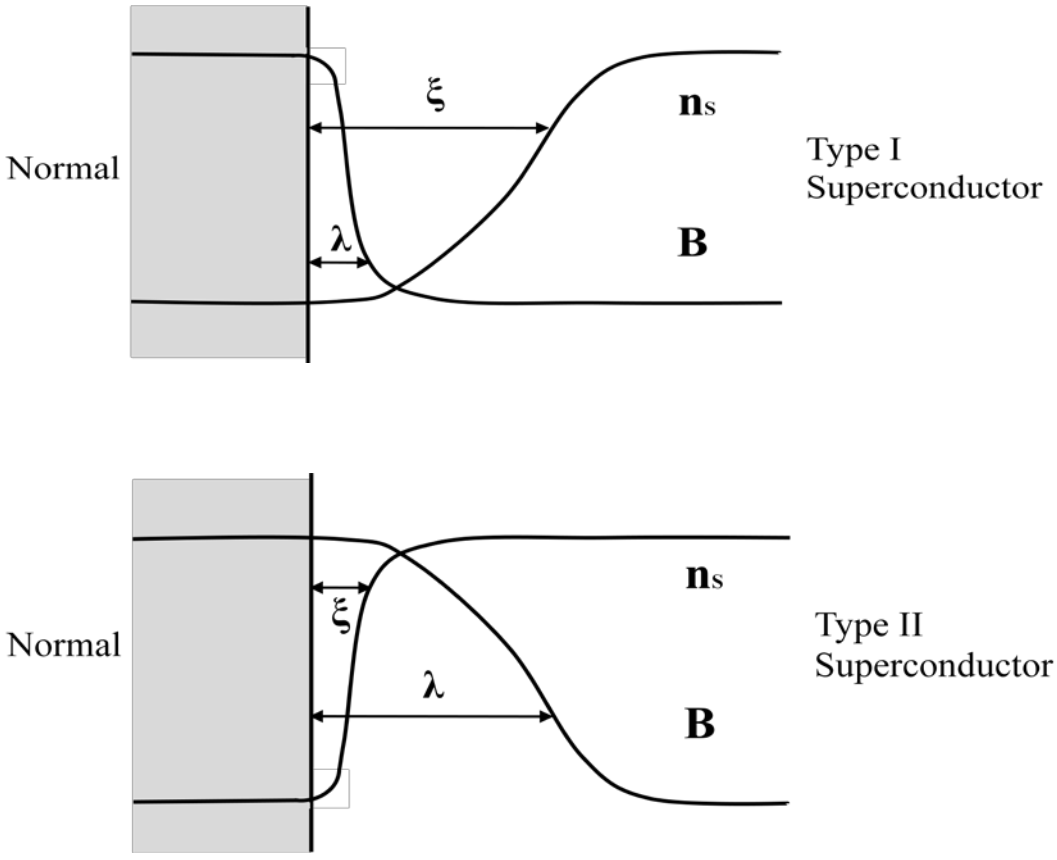

Fig. 7. Variations of the magnetic field B and the density of superconducting electrons at the normal and superconducting interface.

As the external magnetic field increases, or the density of vortices increases, they get closer and begin to repel each other, forming a periodic structure of vortices (Fig.7).

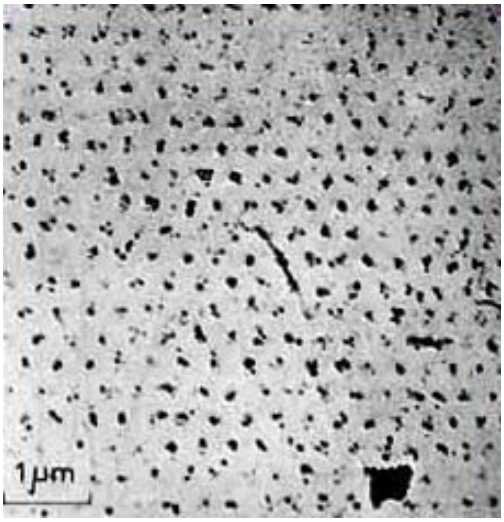

Fig.8. Triangular array of magnetic vortices. The vortices were imaged by a magnetic particle decoration technique. The magnetic field is perpendicular to the film. [4].

Energy Dissipation due to Vortex Motion

Consider that a transport current density $\boldsymbol{J}$ is applied to a superconducting film in the vortex state. The applied magnetic field is in the z direction and the current density is in the y direction (Fig.9).

The current density exerts a Lorentz force, $\boldsymbol{J\hat{y}} \times \frac{\boldsymbol{\Phi_0}}{\boldsymbol{c}}\ \boldsymbol{\hat{z}}$ on the vortices, causing them to move in the x direction [5]. The moving vortex with a velocity $\boldsymbol{V}$ generates an electric field

$$\boldsymbol{E} = \boldsymbol{B} \times \frac{\boldsymbol{V}}{\boldsymbol{C}}$$ in the y direction,

where v, the steady state velocity of the vortex, is obtained from the driving Lorentz force and the friction force.

$$\boldsymbol{F}_{\eta} = -\eta \boldsymbol{V}$$

The electric field which runs parallel to ***J*** gives rise to the power dissipation.

$$\boldsymbol{J} \cdot \boldsymbol{E} = \boldsymbol{J} \cdot \boldsymbol{B} \times \frac{V}{C} = JB\frac{V}{C}$$

Therefore, if the external current exerts a Lorentz force on the vortices and makes them move, there is energy dissipation. In order to avoid energy dissipation due to the vortex flow, the vortices have to be pinned.

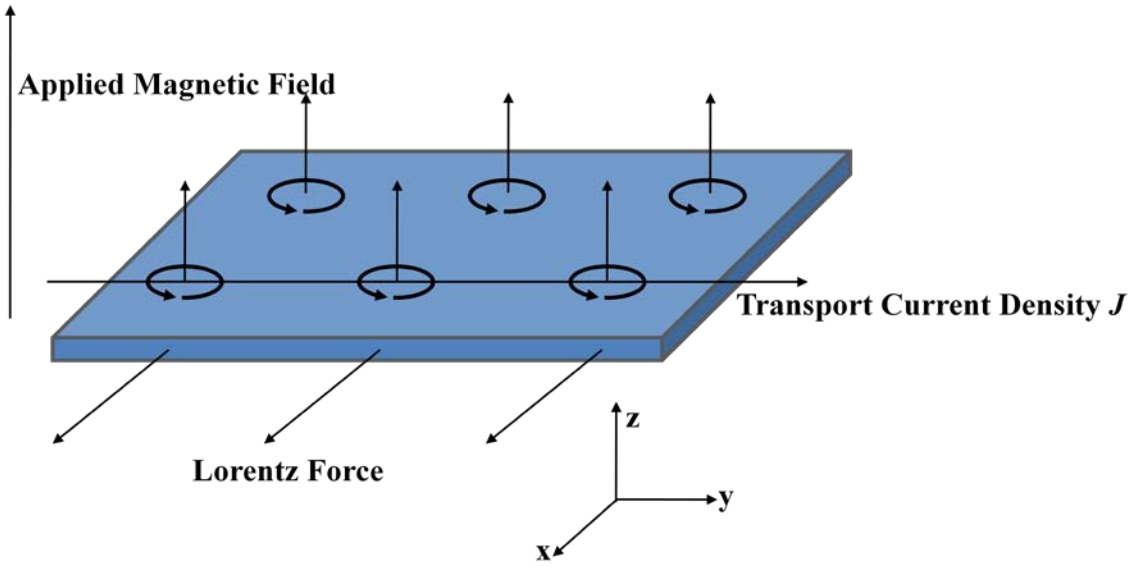

Fig. 9. Vortex motion due to the Lorentz force.

Vortex Pinning in the Ferromagnet-Superconductor Hybrid (FSH)

Magnetism and superconductivity are known to be mutually exclusive to each other. As explained in the previous sections, an applied magnetic field can destroy superconductivity, and superconducting materials, when cooled down below the critical temperature, can exclude an external magnetic field.

But the Ferromagnet- Superconductor Hybrids (FSH) are theoretically predicted to enhance superconducting properties, such as a higher critical current and higher critical field (H_{c2}) than those of original superconductors [6].

When a current is applied to type II superconductors in the mixed state, the vortices, feel a Lorenz force perpendicular to the current and the applied magnetic field. Without a pinning force to balance the Lorenz force, the vortices will move in the direction of the Lorenz force. The motion of the vortices is responsible for energy dissipation in superconductors, restricting practical applications of type II superconductors. In order to increase the current that superconductors can tolerate without energy dissipation, it is necessary to prevent the motion of vortices against the Lorenz force.

Flux pinning in superconductors has been studied both for fundamental physics and for practical applications. In order to enhance flux pinning, many types of ordered defect arrays, such as submicron holes, have been fabricated [7-17]. Most of the defect arrays destroyed the superconductivity locally to attract a vortex core to that region. The core energy, however, represents about 10% of the total vortex energy.

Our group has proposed to use not only the core energy but also the magnetic field energy of the vortex to pin it, i.e. the total vortex energy [18, 19]. Although a homogeneous magnetic field cannot pin vortices, they can be pinned by a Strongly Varying Magnetic Field (SVMF) because the inhomogeneous magnetic field provides barriers for vortex motion.

Previous work on magnetic pinning in superconductors has focused on artificial arrays of pancake-like magnetic dots [20-34]. The component of magnetization from pancake-like magnetic dots is mainly in-plane or parallel to the superconducting film. Flux pinning by submicron size dots with magnetization in-plane was first performed by Martin et al [21]. In the case of magnetization parallel to the superconducting film, studies of transport properties have been performed by Schuller's group [29-34]. Flux pinning by magnetic dots with normal magnetization was shown by Morgan and Ketterson [22].

In contrast to pancake-like magnetic dots, Magnetic Nano Rods (MNR) with a high aspect ratio are desirable for strong magnetization perpendicular to the superconducting film.

To provide a Strong Variable Magnetic Field (SVMF), a triangular array of the cobalt MNR which has a height of 350 nm and a diameter of 100nm was used in the experiments described here. A triangular array with a spacing of 300nm was chosen because the vortices in a type II superconductor prefer to form a triangular lattice [2]. To fabricate the MNR with a high aspect ratio, electron beam lithography and electroplating techniques were used.

On top of the array of MNR, 120nm of Pb_{82} Bi_{18} was thermally deposited at liquid nitrogen temperature to make an embedded FSH system.

With magnetic force microscopy and scanning Hall probe microscopy, we observed that the cobalt MNR preserve the magnetization direction (parallel to the column) even at room temperature [35].

This study showed that the magnetic pinning of the cobalt MNR enhanced the superconductivity of Pb_{82} Bi_{18} in the embedded FSH system, i.e. increased the critical current and the critical field (H_{c2}). For comparison, the FHS system and a control sample with out MNR were prepared on a single substrate (Si/SiO_2). In addition to the enhancement of superconductivity, the embedded FSH showed the field matching effect, the compensation effect and the magnetic hysteresis.

The field matching effect is due to the increase in pinning when the vortex lattice is commensurate with that of pinning centers [22, 34]. When the applied magnetic field generates integer multiples of flux quantum per unit cell of pinning sites, the pinning becomes stronger, showing periodic oscillations in the resistance and the critical current. A decrease in resistance and an increase in the critical current was observed when the applied magnetic field values were integer multiples of a flux quantum per unit cell of pinning sites. According to stability simulations [36], for weaker pinning, a second peak (pronounced increase in the critical current at the second matching field, is absent in a triangular array of pinning sites. However, the embedded FSH showed not only the first matching but also the second matching effect, implying that the MNR provides a strong pinning of the vortices.

It was also observed that the stray magnetic field from the MNR effectively reduced an applied external field in parts of the superconducting film (compensation effect), thereby allowing the film to still carry a superconducting current in higher magnetic fields [19] (Fig.10). Both the resistance and critical current of the embedded FSH showed hysteric behavior under the field-sweep measurement because of hysteresis of the nanorod magnetization.

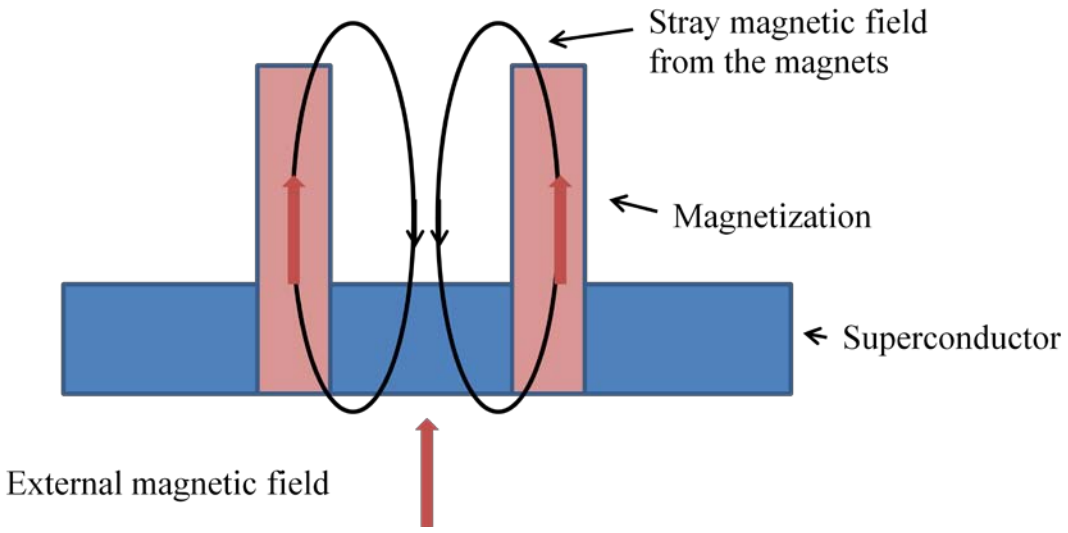

Fig.10. A schematic of the field compensation effect.

CHAPTER II

FABRICATION OF EMBEDDED FERROMAGNET-SUPERCONDUCTOR HYBRID SYSTEMS

This chapter explains how embedded ferromagnet-superconductor hybrid systems were fabricated: a superconducting film on top of magnetic nanostructures. First, fabrication methods of magnetic nanostructures are described. Specifically, electron beam lithography and the electroplating technique are reviewed, including structural characterization with scanning electron microscopy (SEM) and atomic force microscopy (AFM). Then fabrication of contact pads, cathodes, electrical leads to the cathodes, and superconducting films are discussed. In particular, how to configure the photo mask pattern of two systems on a single substrate, where each system consists of four contact pads and an electrical lead to a cathode, is explained. The schematic diagram (Fig.11) shows the steps for fabricating embedded ferromagnet-superconductor hybrids (FSH). Fig.12 shows the process of fabrication of cobalt nanorods, corresponding to steps 2 through 7 in Fig.11.

1. Contact pads for four wire measurement and electrical leads to the cathode by photolithography

2. Thermal deposition of Cr (~2nm) and Au (~50nm)

3. Patterning a mask for Au film cathode for electrodeposition and cohesion frames for a superconducting film by electron beam lithography

4. Thermal deposition of Cr (~2nm) and Au (~25nm)

5. Patterning triangular arrays by electron beam lithography

6. Electrodeposition of cobalt

7. Removal of PMMA

8. Pattering a mask for a superconducting film by electron beam lithography

9. Thermal deposition of Pb_{82} Bi_{18} on top of the cobalt structure: hybrid system

Fig.11. Fabrication steps for an embedded ferromagnet-superconductor hybrid system.

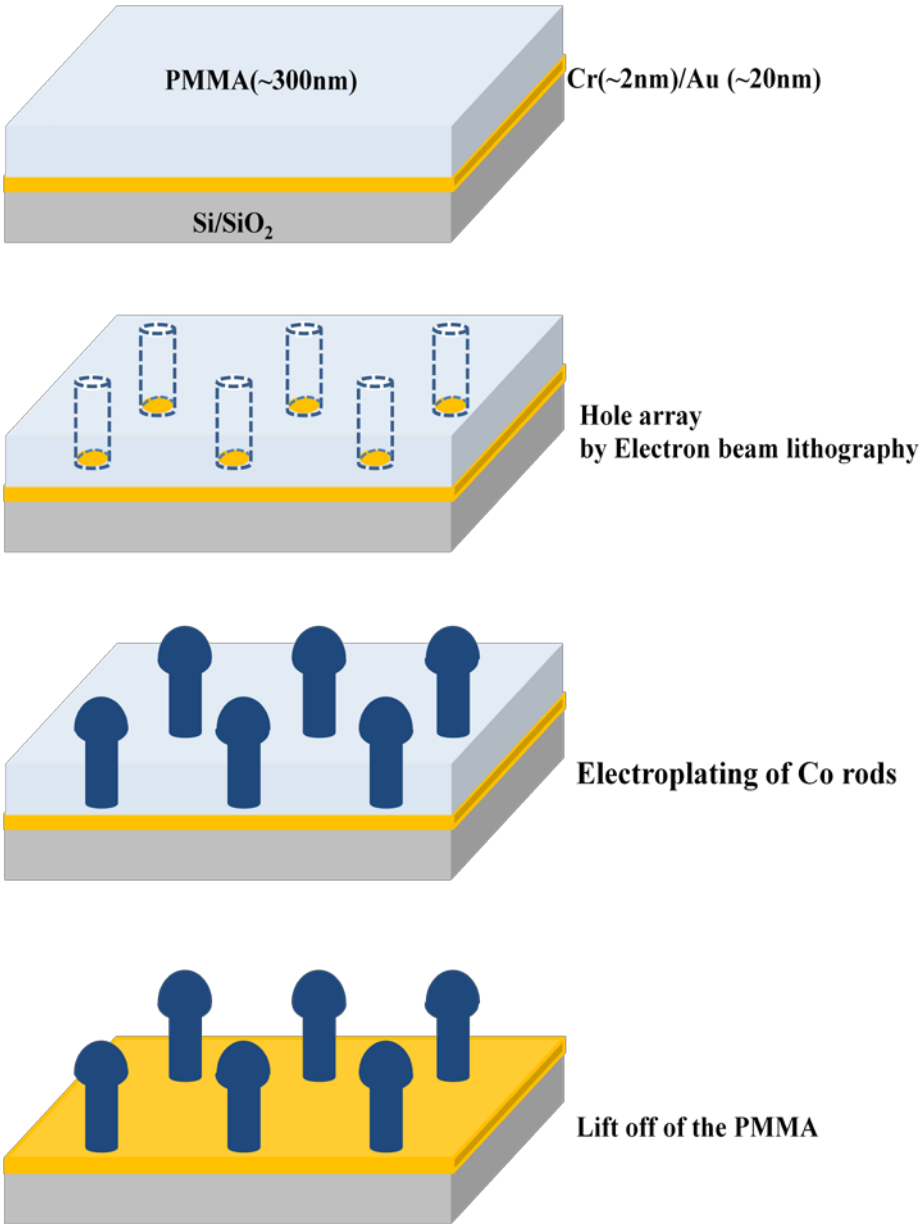

Fig. 12. Illustration of fabrication of cobalt nanorods by e-beam lithography and electrochemical deposition.

Electron Beam Lithography

Several new lithographic techniques to fabricate nano-sized structures, including X-ray lithography [37-40], scanning tunneling microscopy-assisted techniques [41-44] and electron beam lithography [45-51] have been developed. Electron beam lithography is one of the most widely used lithographic techniques for fabricating nano-sized structures. Electron lithography uses electron beams of a scanning electron microscope (SEM) to define the desired patterns.

A detailed process of electron beam lithography for patterning a triangular array of circular holes in a polymethylmethacrylate (PMMA) matrix follows. In the first step, the pattern of triangular array of holes with 20 nm in diameter was drawn with Computer-Aided Design (CAD) program. The triangular array and high aspect ratio of the nanostructures were chosen to explore the transport measurement of ferromagnet-superconductor hybrid systems. The detailed explanation for the choice will be given in chapter IV. The triangular array for the holes was drawn on 100 μm × 100 μm a square in the CAD program. In order to make structures with a high aspect ratio, the holes of diameter 20 nm were drawn in the CAD program, but the actual diameter after electron beam lithography turned out to be 100 nm because of the electrons scattered inside the PMMA [52,53]. Fig.13 shows a SEM image of one of the fabricated triangular arrays of cobalt nanorods with a diameter of 100nm.

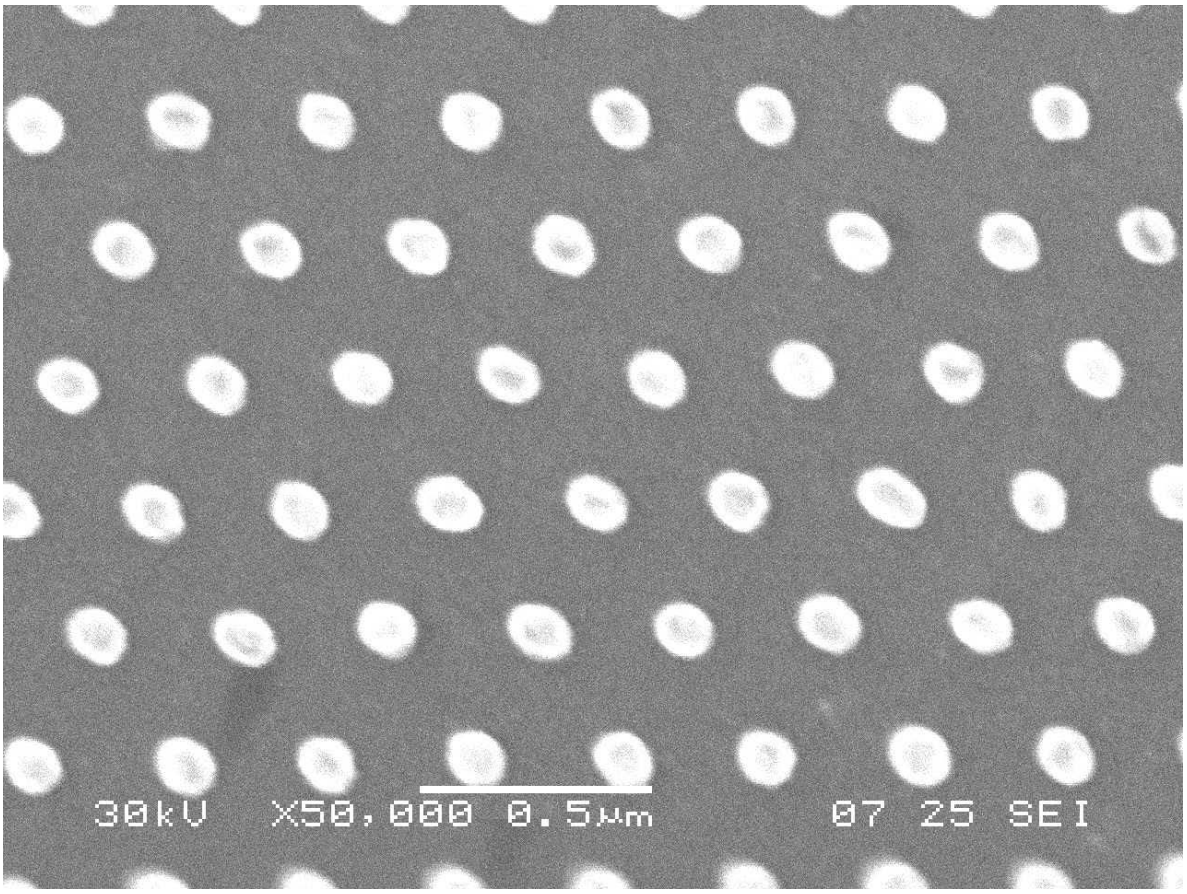

Fig. 13. SEM image of a triangular array of cobalt nanorods

(300nm spacing between the 100nm diameter rods).

In the second step, 950K (Monochlorobenzene, 3%) PMMA resist was spin-coated onto a Si/SiO_2 substrate at 1500 rpm for 60 s, resulting in a 350nm thick layer. The sample was then baked on a hot plate at 120 ^{o}C for 1 min. In the case where thicker PMMA layers for higher structures are needed, the rpm for spin coating can be lowered, or PMMA can be spin coated repeatedly. Fig. 14 shows the increased height of rods formed by repeating the spin-coat of PMMA.

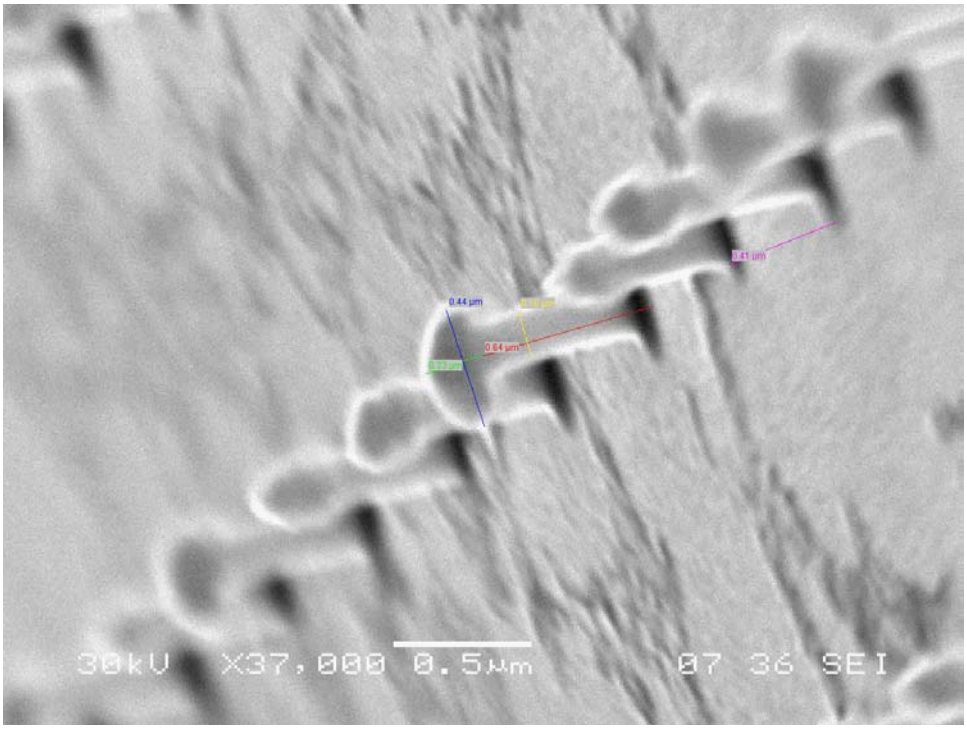

Fig. 14. The height of the structure is measured to be about 640 nm and the diameter about 160 nm, giving an aspect ratio of 4. The height of the overgrown caps at the top is about 230nm and their diameter can have a maximum up to 440 nm.

In the third step, after optimizing the focus, the pattern programmed in CAD was drawn with the electron beam of a SEM onto the Au film cathode for electrodeposition of the Co nanorods which was defined by electron beam lithography, followed by thermal deposition of a thin Cr adhesion layer and then thermal deposition of the Au cathode on the Si/SiO_2 substrate. The details of fabrication of the cathode on the Si/SiO_2 substrate will be discussed later in this chapter. A 100 μm × 100 μm array of holes for the nanorods was patterned and repeated three times to give the whole pattern (300 μm ×100 μm) (Fig.15). The reason for repeating each square pattern rather than patterning the whole rectangle with holes is that the small pattern area can make the deflection of the beam small and thus can maintain the focus which has been optimized. The electron beam of a JEOL-JSM 6460 used a 30 kV accelerating voltage, and the beam current value was chosen at 10 pA.

Finally, the sample was dipped into the customary developer (1:3 Methyl Isobutyl Ketone/2-propanol) for 1 min and then rinsed in 2-propanol. After completion of these steps for electron beam lithography, the sample was ready for the next step: electroplating or electrodeposition.

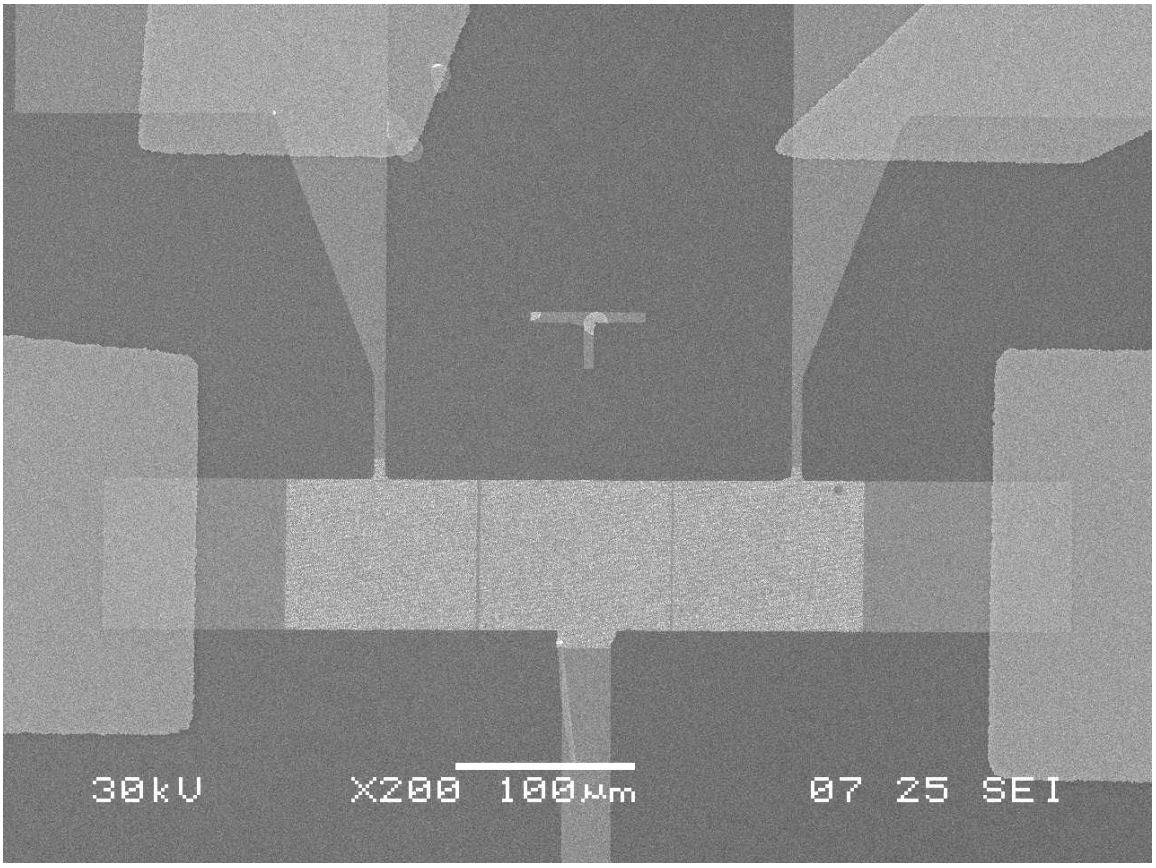

Fig. 15. SEM image of the whole pattern (300 µm ×100 µm). The center section shows the three 100 µm ×100 µm arrays of plated Co nanorods on a triangular lattice above the Au film cathode. The electrical contacts for the four terminal transport measurements and the contact lead to the cathode are visible through the PMMA.

Electroplating

In this section, the motivation for the electroplating technique and its advantages and disadvantages are discussed, especially comparing it with thermal deposition, one of the most common deposition methods.

The electroplating, also called electrodeposition, technique was first invented by chemist Luigi V. Brugnatelli in 1805, and the method has been utilized routinely to fabricate nanostructures [54- 57]. Compared with the thermal deposition method, the electroplating technique enables a high aspect ratio metallization of iron (Fe), cobalt (Co), nickel (Ni), and their alloys [58,59,60]. The thermal deposition method is not suitable for making a high aspect ratio structure of Fe, Co, and Ni. The reasons are that Fe, Co, and Ni have high melting points and that thermal deposition does not transfer the pattern in the polymethylmethacrylate (PMMA) matrix. This is called the shadowing effect (Fig.16). Also shadowing in thermal deposition can cause the whole film to peel off during the lift-off process. Unlike thermal deposition, the electroplating method does not need to melt the magnetic materials and does not exhibit a shadowing effect.

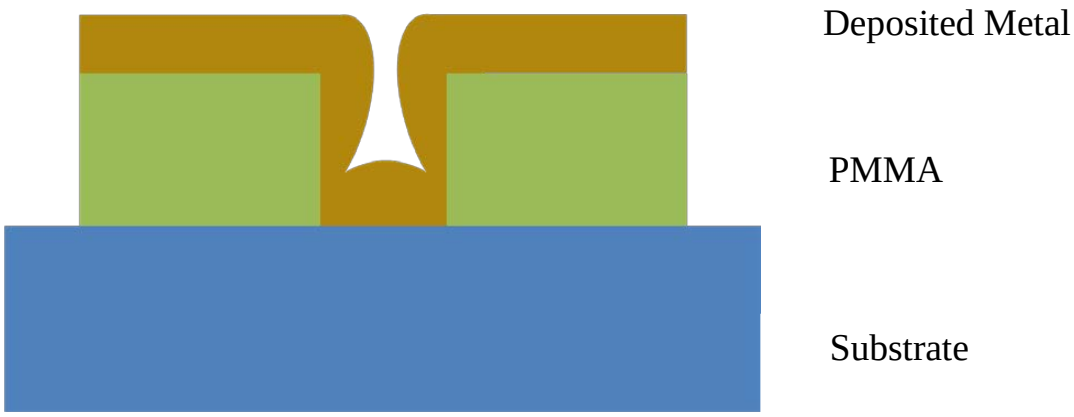

Fig. 16. The shadowing effect associated with thermal deposition through the patterned holes in the PMMA.

Electrodeposition is the process of producing a metallic coating on a metal surface by passing an electric current in an electrolyte solution. The electrodes consist of the anode and the cathode. The pole at which oxidation takes place is the anode while the pole at which reduction takes place is the cathode. When voltage biased, positive ions in the solution are deposited onto the negatively charged plate or cathode. In our experiment, cobalt was deposited onto a gold film with a PMMA template which was patterned by electron beam lithography. A cobalt metal sheet was used as the anode or counter electrode. Fig. 17 shows a schematic of the electroplating deposition of cobalt material.

Below is the reduction reaction where cobalt is deposited on the cathode:

$$Co^{2+} + 2e^{-} \longrightarrow Co\ (s)$$ electrolyte solution: ($CoCl_2.6H_2OH_3BO_3$)

The electrolyte for Co plating was prepared with 100 g/ L of cobalt (II) chloride hexahydrate ($CoCl_2.6H_2O$) and 60g/L of boric acid (H_3BO_3) [61]. The boric acid was used to keep the pH level of 2.5 – 3.5.

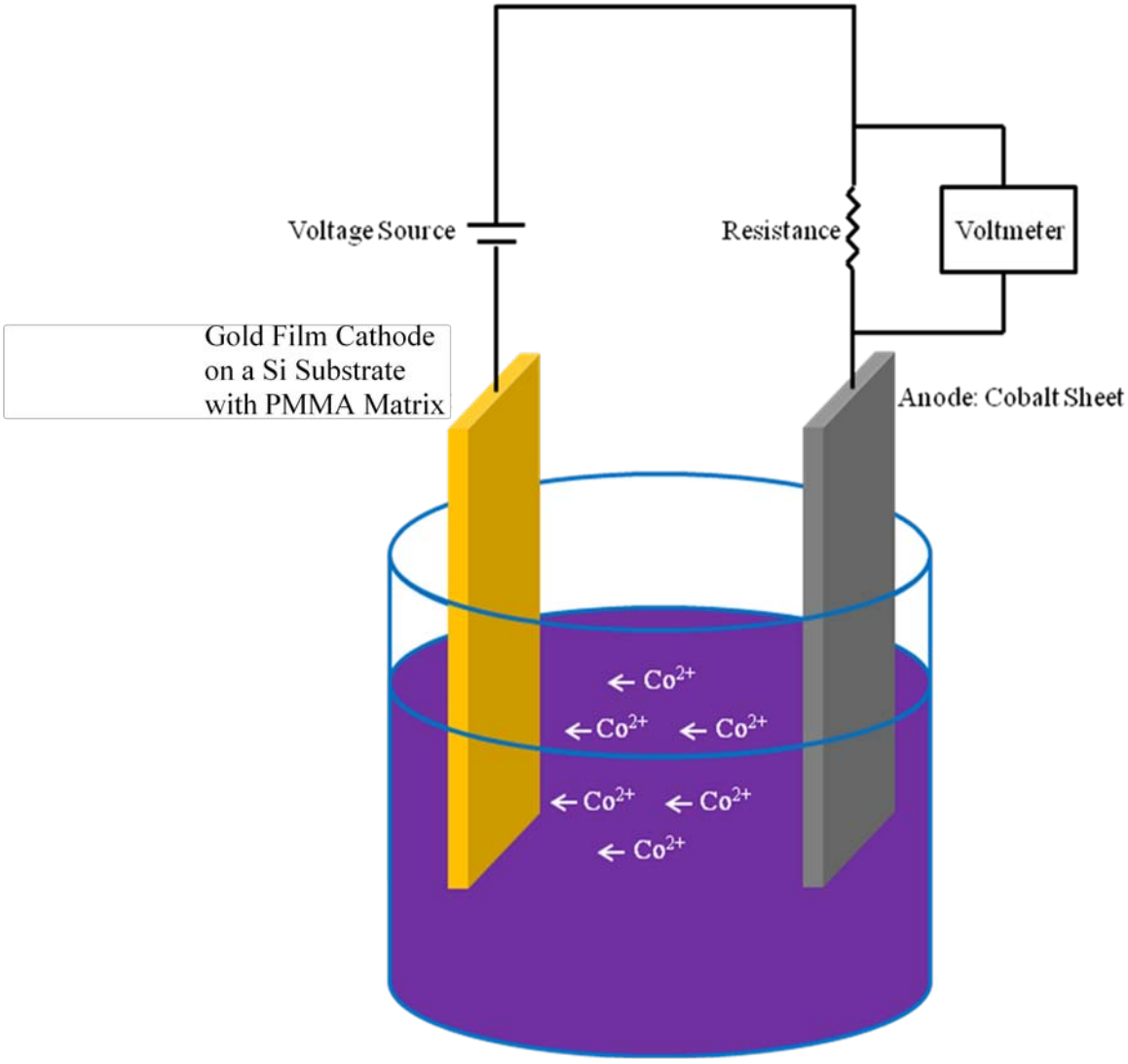

Fig. 17. Illustration of the experimental setup of the electroplating deposition.

The detailed process of electro chemical deposition of cobalt nanorods follows. In order to prepare the Au film cathode for the electroplating process, a thin film of Au (~25nm) was deposited onto a Si/SiO2 substrate by thermal evaporation at a chamber pressure of ~3×10^{-6} torr after depositing a cohesion layer, Cr (~2nm).

The mask was designed for the cathode and for a cohesion frame for the subsequently deposited superconducting film. The cohesion frame bridged the cathode and the contact pads. While depositing the cathode, the cohesion frame was deposited at the same time. The detailed explanation of this mask will be given later in this chapter.

After making the triangular array in the PMMA matrix, the sample was immersed in the Co solution for electroplating. A small portion of the PMMA film at the end of the electrical lead to the cathode was removed to permit electrical contact to the battery.

The time required to electroplate the Co nanorods to slightly overfill the holes created in the PMMA resist was estimated by repetition of a sequence of short growth periods. Each of these short periods lasted only a few seconds at a plating current of 0.1~0.5 μA. Following each of these growths, the surface of the pattern area was checked with an optical microscope. This process was continued until the nanorod array could be detected. The total growth time for slightly overgrown Co nanorods depends on the overall size of the e-beam patterned area, the diameter of the individual holes, and the density of the array. The slightly overgrown rods form mushroom-shaped structures or caps (Fig. 18). The caps of the structures can shadow the substrate and prohibit the subsequently evaporated superconducting film from depositing on the magnetic structures, preventing the proximity effect between magnetic Co nanorods and the

superconducting film. It is important, however, that since the superconducting film will be deposited directly onto the Au cathode after removal of the PMMA, there will be a proximity effect between it and the Au film.

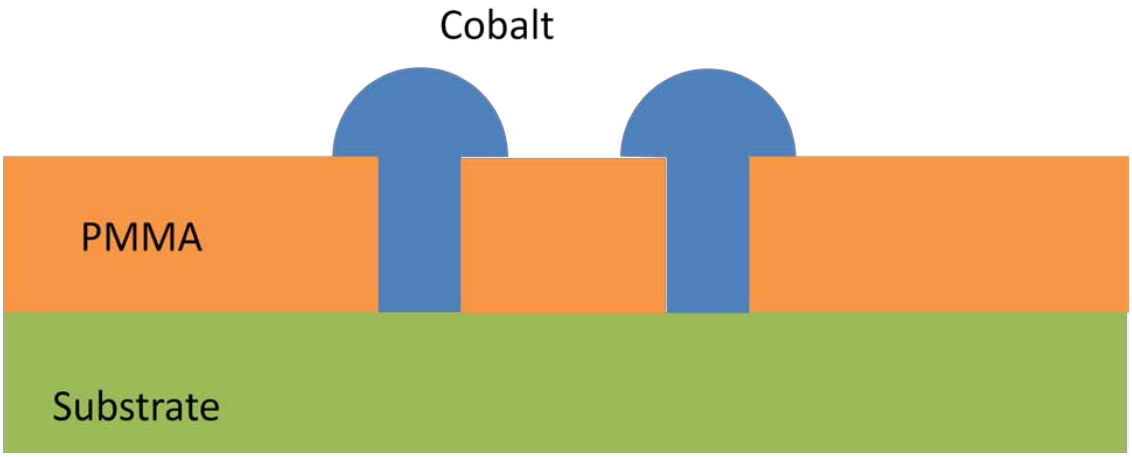

Fig. 18. Overgrown cobalt nanorods with mushroom-shaped structures or caps.

The resulting specimen was then immersed in acetone to remove the PMMA resist for Atomic Force Microscope (AFM) and Scanning Electron Microscopy (SEM) characterization. As a final step to form an embedded FSH, a film of Pb_{82} $Bi_{18.}$ (about 120nm in thickness) was deposited on top of the array of Co MNR.

Before discussing the thermal deposition of the superconducting film, several difficulties of electroplating and the possible solutions to those difficulties are described. One of the biggest challenges is to find optimal parameters for the current and time.

Besides estimating the time by repetition of a sequence of short growth periods, we used the integrated value from the graph of current $I(t)$ as a function of time. The total amount of deposited material is theoretically proportional to this integral. A LabView program was used to monitor the current with respect to time while electroplating cobalt. Fig.19 shows a sample of cobalt rods and the corresponding the current-time graph for their growth. Fig.20 shows the overgrown structures due to the excessive value of the current and time.

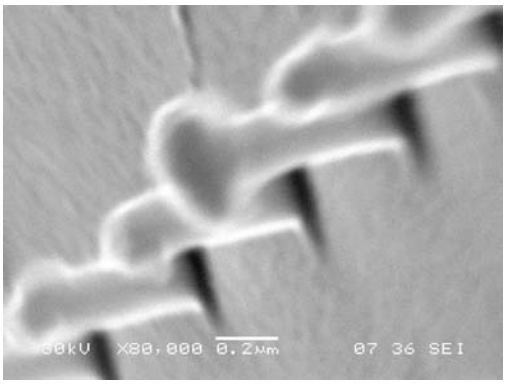

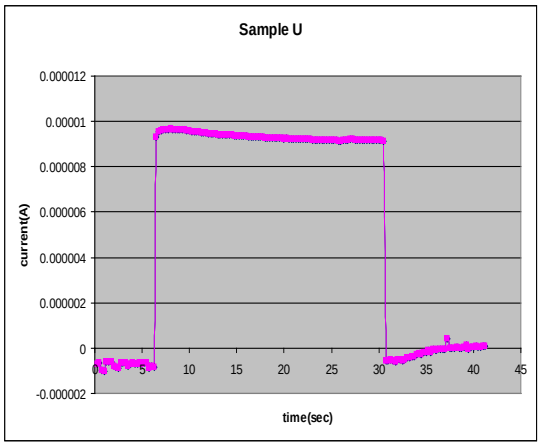

Fig. 19. The area in the current-time graph represents the amount of the deposited material for the array of Co nanorods shown in the SEM image above.

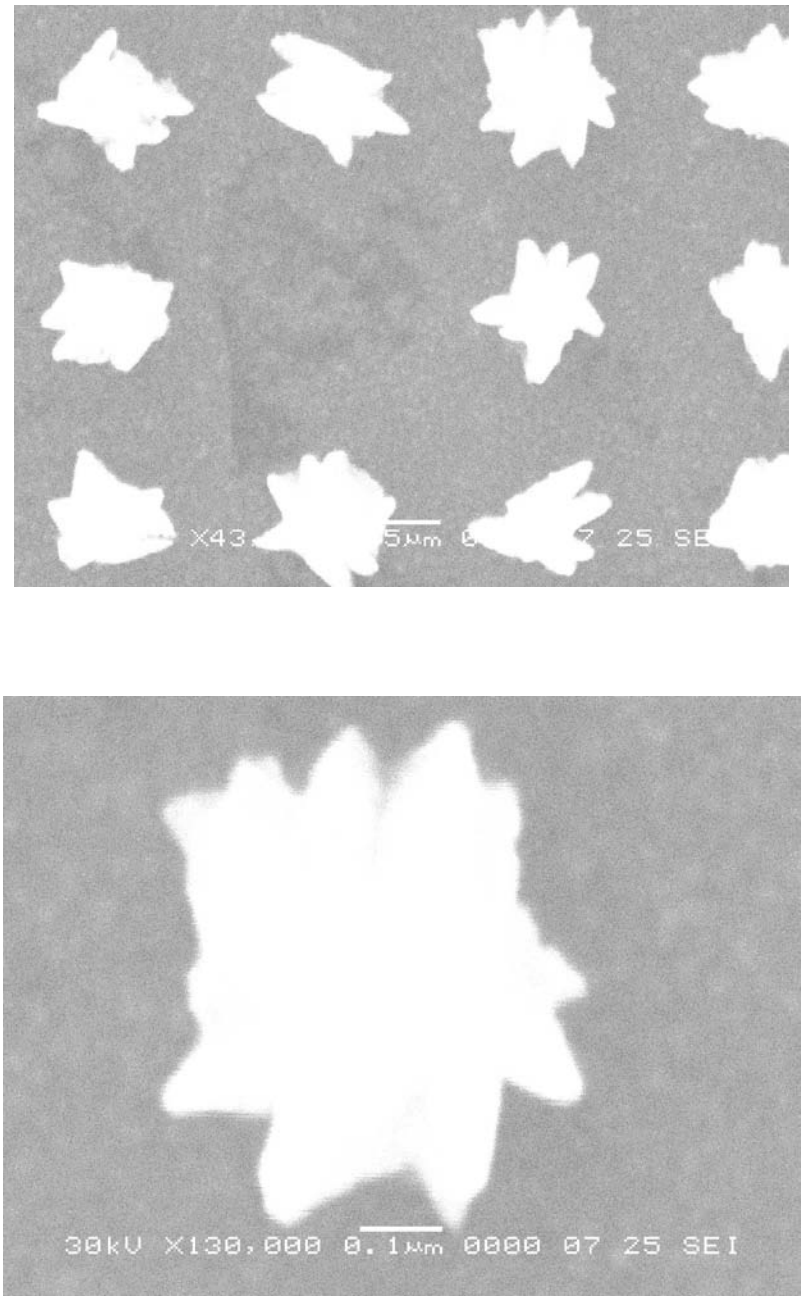

Fig. 20. SEM images of irregularly overgrown structures.

In addition to finding the appropriate parameters for the current and time, another difficult problem of electroplating is to make a uniform deposition. The uniformity problem usually arises in the process of electron beam lithography. Some of the holes in an array may not be fully patterned (Fig.21).

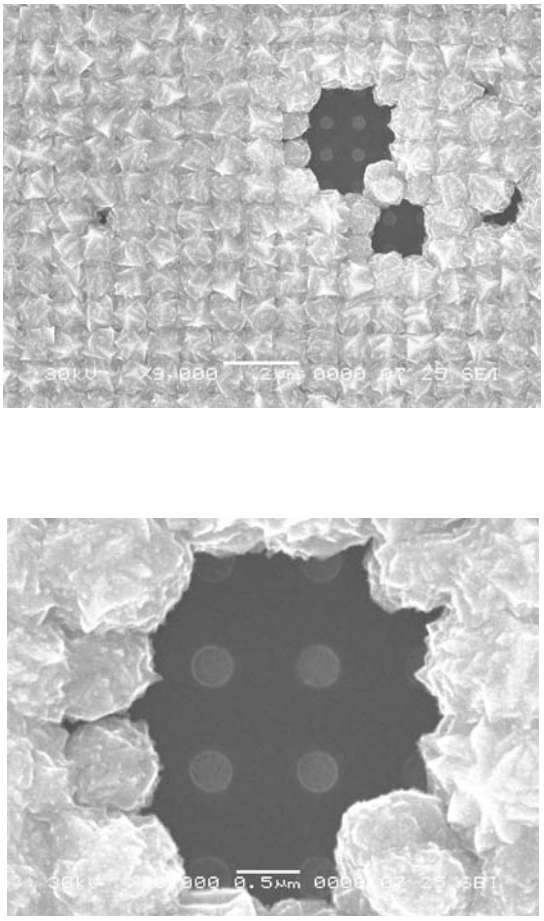

Fig.21. The bottom SEM picture shows an expanded view of the larger area of unplated Co rods shown in the upper SEM image of a large array of Co nanorods. The light regions are the caps of the overgrown rods, but four holes that were not filled during plating can readily be seen in this area.

A possible factor that can cause unfilled holes is improper focus due to the deflection of the electron beam. The deflection in the process of patterning can be minimized by reducing the pattern area or using a high magnification in the SEM. For good focusing, T-shaped structures were patterned 125 μm from the cathode film. Also unfilled holes may be caused by a thin or irregular cathode Au film. If the Au film cathode is too thin or not does not deposit in some small area, the positive Co ions cannot be deposited in that region. From the experiment, a Au film turned out to be better suited for a uniform cathode film than was a Ag film. The best results were found with Au films greater than 20 nm in thickness.

A minor complication in the electroplating process is that sometimes the structures grow in an area where they are not wanted. For example, magnetic structures may occasionally grow on the contact pads (Fig.22). The possible reasons are that the PMMA did not spin coat on that area and that the silicon substrate was not perfectly insulating. This problem may be avoided by spin coating a thicker PMMA layer and by checking the conductivity of the silicon substrate.

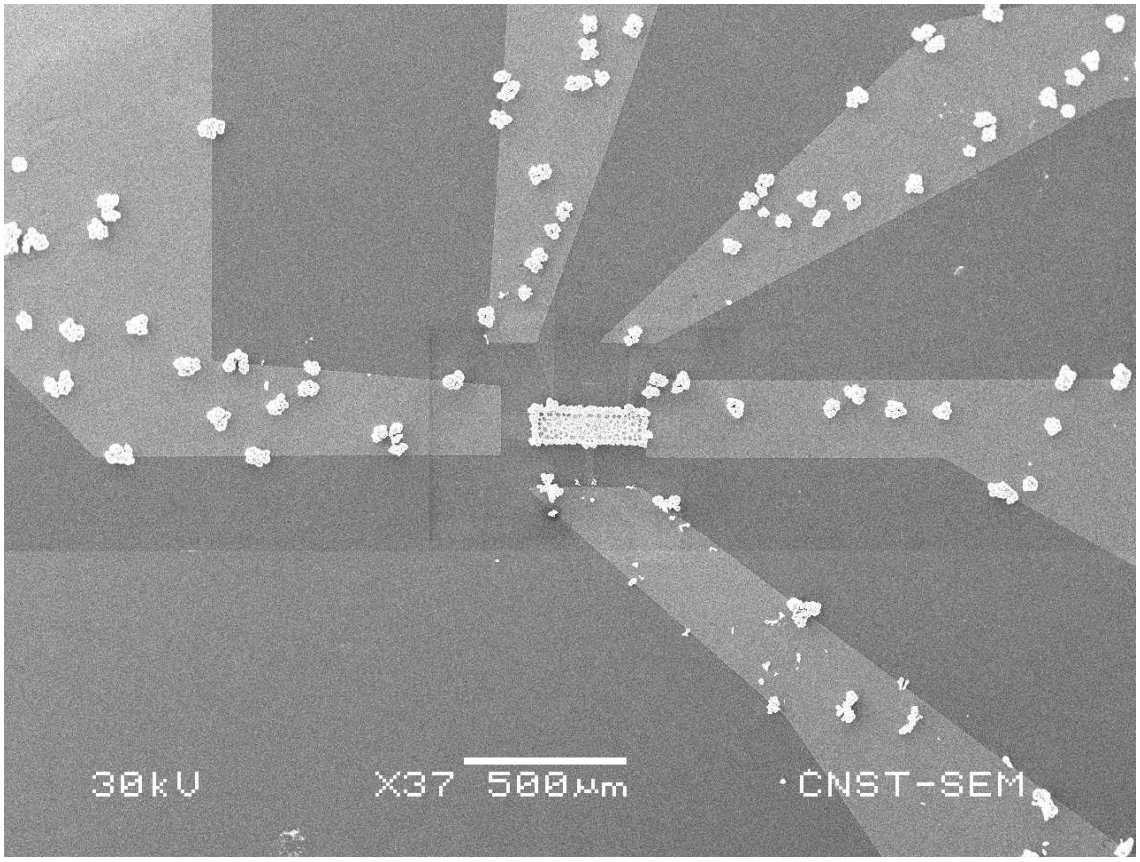

Fig. 22. Cobalt was grown not only on the Au film cathode, but also on the contact pads for this sample.

Thermal Deposition and Mask Fabrication

In this experiment, the thermal deposition method was used in several steps of fabrication: contact pads for four wire measurements, electrical lead to the cathode, the cathode, the cohesion frame, and finally the superconducting film. Electron beam lithography and photolithography were employed to fabricate the masks, depending on the feature size of the patterns.

Thermal deposition and photolithography method were used to fabricate contact pads and the electrical lead to the cathode. The photomask was designed to accommodate both an embedded FSH and a control sample (a Pb_{82} Bi_{18} film on Au) on a single substrate (Fig.23). Attention was paid to making the electrical lead to the cathode as long as possible. To ensure that the sample was immersed deep inside the solution, the electrical leads to the cathode were chosen to be diagonal.

Below is the process of photolithography for patterning the mask on a Si/SiO_2 substrate. First, photoresist (SC 1805) was spin-coated on a Si/SiO_2 substrate at 5000 rpm for 60 s, resulting in a 500 nm thickness. The sample was then baked on a hot plate at 120^oC for 1 min. The photoresist and the parameters were chosen by consideration of the resolution and the uniformity: the thinner, the better resolution and the thicker, the fewer unwanted pinholes in the photoresist. The sample with the mask on it was exposed to an ultraviolet (UV) laser for 2s. Finally, the sample was dipped into the developer (MF 319) for 40s and then rinsed in deionized water. To complete the pattern by photolithography, layers of Cr (~2nm) and Au (~50 nm) were thermally deposited, followed by lift-off of the photoresist.

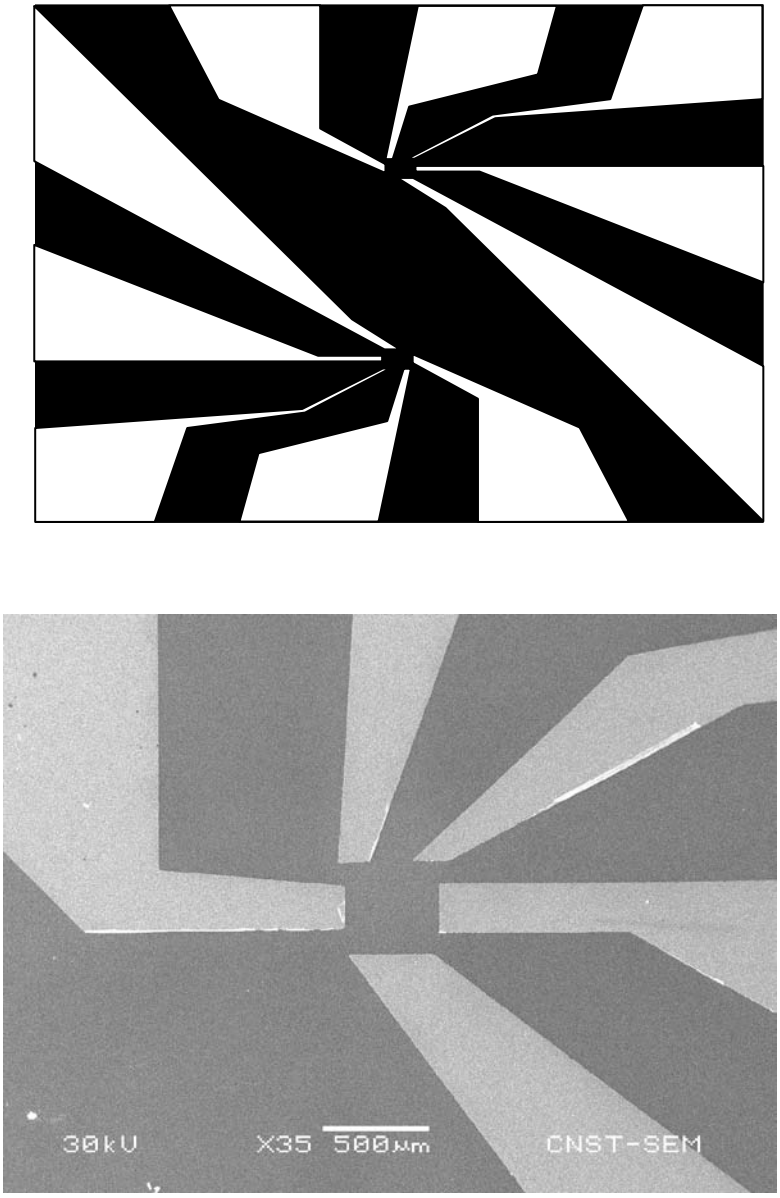

Fig. 23. A photo mask (1 cm by 1cm) for the Au contact pads and electroplating contact for dual samples and the SEM image of the completed pattern for one of these samples. The electrodes are the light region with the current leads and the two voltage leads for four terminal transport measurements on each side and at the top of the sample area, respectively, and the electroplating contact at the bottom.

For the Au film cathode and the cohesion frames, the mask was patterned by electron beam lithography, followed by sequential thermal deposition of Cr (~2nm) and Au (~25 nm) films (Fig 23). In this pattern, the T-shaped structure which is125 µm above the Au film cathode is designed for the location of focus, or e-beam spot during the beam focusing step. The thickness of Au was chosen to be thick enough to ensure the uniformity for electroplating and thin enough to reduce the proximity effect between the Au cathode and the superconducting film which was later deposited on it after electroplating the Co nanorods. The cohesion frames turned out to be critical in adhesion of the superconducting film to the substrate.

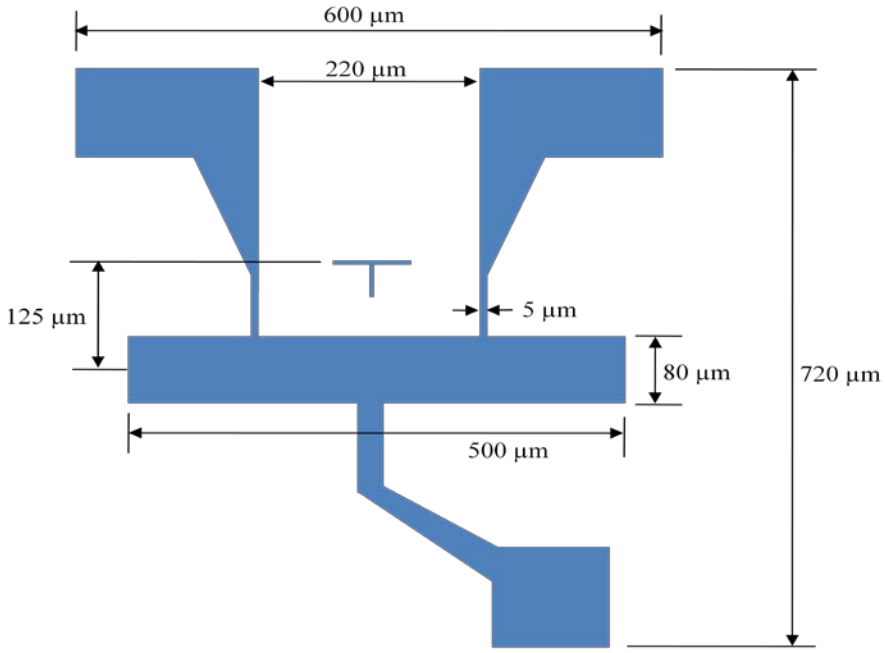

Fig. 24. The pattern for electron beam lithography of the cathode, cohesion frames, and electrical lead to the cathode. The rectangle (80 µm ×500 µm) is for the Au film cathode and the thin part (5 µm) is for the cohesion frame.

Finally, the mask for the superconducting film was patterned by electron beam lithography. The wider part from the overlap of the contacts pads to the film was designed to allow a smaller current density than that in the FSH film, maintaining superconductivity in the bare film (Fig.25). The source for evaporation of the superconducting film, bulk ingot of Pb_{82} Bi_{18} was prepared by arc melting in an argon atmosphere. To ensure a smooth, high quality film, the superconducting film was deposited at liquid-nitrogen temperature and in a vacuum level of ~10^{-7} Torr. The film thickness (120 nm) was determined during deposition with a quartz crystal microbalance (QCM).

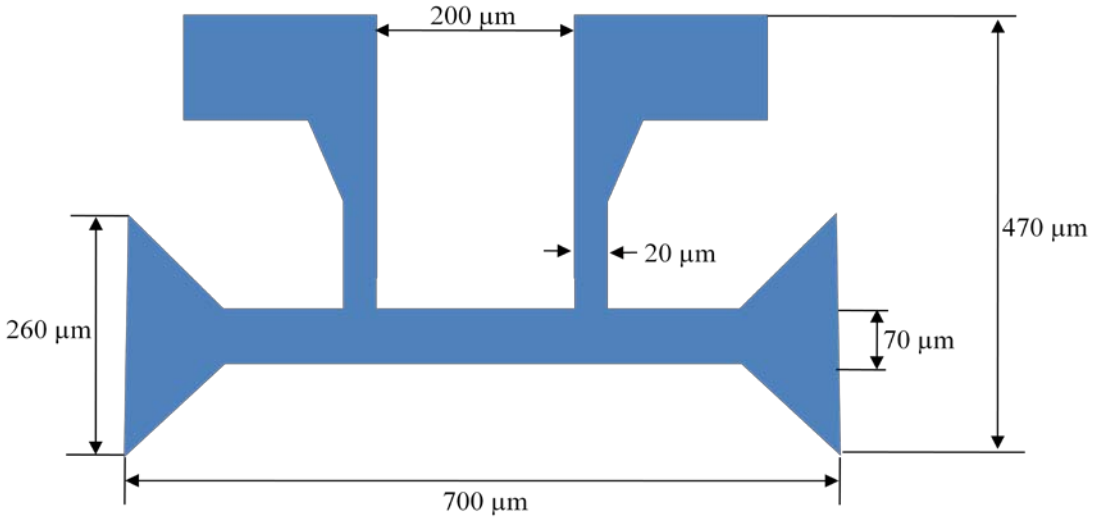

Fig. 25. The pattern for electron beam lithography for the superconducting film and the contact pads.

CHAPTER III

CHARACTERIZATION OF MAGNETIC STRUCTURES WITH MAGNETIC FORCE MICROSCOPY

This chapter explains how to characterize the cobalt magnetic nanorods with the Magnetic Force Microscope (MFM). Starting with the principles of the Atomic Force Microscope, the principles and advantages of the MFM are reviewed. In particular, how the MFM separate the pure magnetic information from any other interactions such as atomic interaction and Van der Waals forces between the tip and sample surfaces is explained. In this study, the MFM measurement with the supplement of Scanning Hall Probe Microscopy (SHPM) showed that each nanorod stays in a single domain (vertically magnetized) in zero field at room temperature.

Principles of Magnetic Force Microscopy

Scanning Probe Microscopes (SPMs) cover several related instruments used to image and measure properties of material surfaces. SPM images are obtained by scanning a sharp probe over a surface under investigation. During the scan over the surface, the interaction between the tip and the surface is displayed as a function of the probe position. The two most common SPMs are scanning tunneling microscopy (STM) and atomic force microscopy (AFM) [62-65]. STM uses the electrical current between the probe and a material surface to image the surface with atomic resolution. Because the STM requires electrical conductivity of the sample surface, it limits the materials that can be studied. AFM, however, can investigate a wide range of materials, not only

conducting materials but also insulating materials. To provide the topography of surfaces, AFM uses the Van der Waals force and electrostatic forces between a cantilever tip and the surface under investigation and measures the resultant cantilever deflection. A position sensitive detector (PSD) of the AFM collects laser light reflected off the back of the cantilever in order to show the image of the topography (Fig.26).

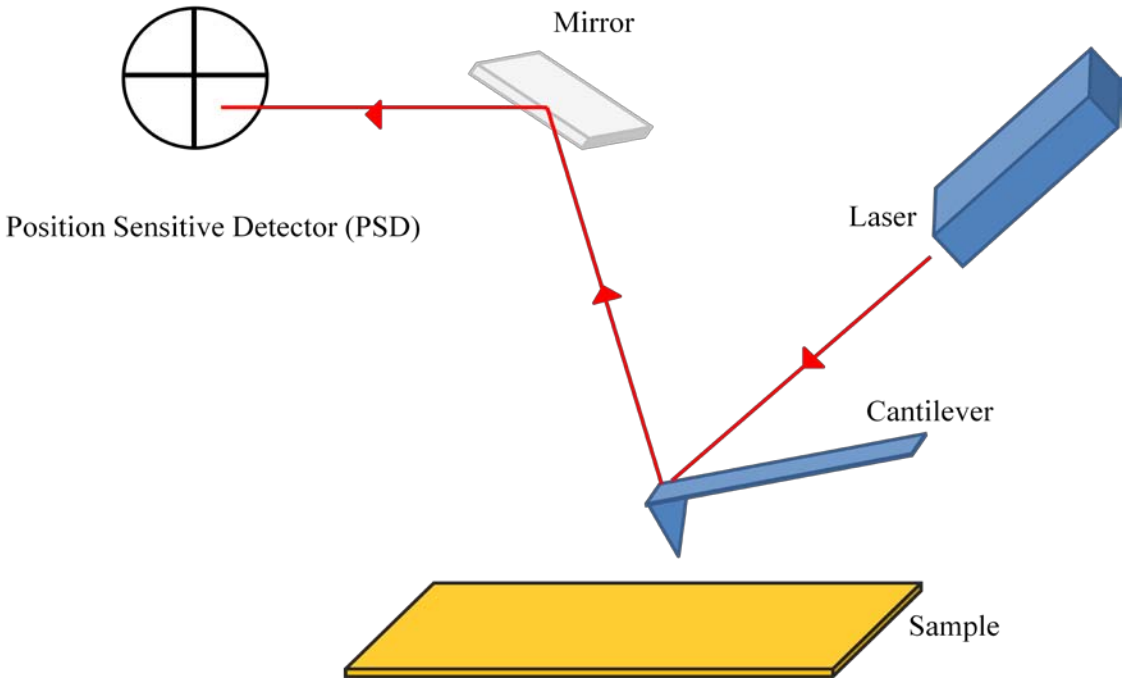

Fig.26. Schematic illustration of the basic components of an AFM or MFM.

There are three operation modes in AFM: contact mode, non-contact mode, and tapping mode. While the contact mode has advantages such as atomic resolution, it can change the properties of the surface because it requires the tip to touch the sample surface. Although the non-contact mode is suitable for studying soft samples, its lateral resolution is limited by the distance between the tip and the sample. Finally, in the tapping mode, or intermittent contact mode, the tip lightly taps the surface at the lowest point of oscillation of the cantilever. In addition to minimizing the contamination of the sample surface, the tapping mode has good lateral resolution of 1 to 5nm.

The MFM is a specific type of the AFM with the capability to investigate magnetic properties of sample surfaces [66, 67]. The tip of the MFM is a Si tip which is coated with a ferromagnetic material. While the spatial resolution of the MFM (10 to 100nm) is considerably worse than that of the AFM (0.02 to 0.1 nm), the force resolution of an MFM (10^{-13}N/m) is considerably better than that of the AFM (10^{-5} N/m) [68].

The MFM has been one of the most widely used magnetic imaging techniques [69-75]. Several advantages include: the spatial resolution of 10~100nm ; the force resolution of 10^{-13}N/m; no requirement for a vacuum environment; operation in a wide temperature range; and no requirement for special sample preparation, such as coating a conducting material [76].

The MFM measures the force that the stray magnetic field from the surface exerts on a tiny magnetic tip attached to a flexible cantilever. The forces exerted on the magnetic tip, however, include not only magnetic forces ($d < 1\ \mu m$) but also other forces such as Van der Waals forces($0.2 < d < 10$ nm), where d is the distance between the tip and the

sample surface. Therefore, in order to separate the long range magnetic forces from the short range Van der Waals forces, the MFM scan uses the TappingMode/LiftMode™ interleave technique developed by Digital Instruments. The first scan is performed in the tapping mode and the second scan at a lifted height is in the lift mode.

The first scan with a lower scan height gathers information about the topography of sample surfaces. The main interactions of the first scan are short range atomic interactions and Van der Waals forces between the tip and sample surfaces. The first scan has to operate in the tapping mode of AFM because the contact mode of AFM, one of the most commonly used modes, can damage the sample surface or change the magnetization. In the tapping mode, the cantilever oscillates with its resonance frequency and only touches the sample at the bottom of each oscillation, thereby minimizing the contamination of the tip and the sample surface.

During this first scan in the tapping mode, the interaction between the tip and the sample causes a change in the amplitude, in the resonance frequency and in the phase of the oscillation of the cantilever. The electronic feed back loop installed in the AFM makes the amplitude of the oscillation constant by moving the scanner in the z direction. The vertical adjustment of the scanner in the z direction provides the height image or the topography. The topography obtained by the first scan is then used as a reference for the second scan.

After the first scan, the cantilever is lifted above the sample to a distance set by the operator and follows exactly the topography traced at the first scan (Fig.27). During this second scan, the tip is maintained at the same distance from the sample surface. As this

fixed distance between the tip and the sample is increased, the magnetic information becomes apparent because the Van der Waals force is a very short range force; whereas, the magnetic force is much longer range. Thus the lift mode makes it possible to image the long range magnetic interactions.

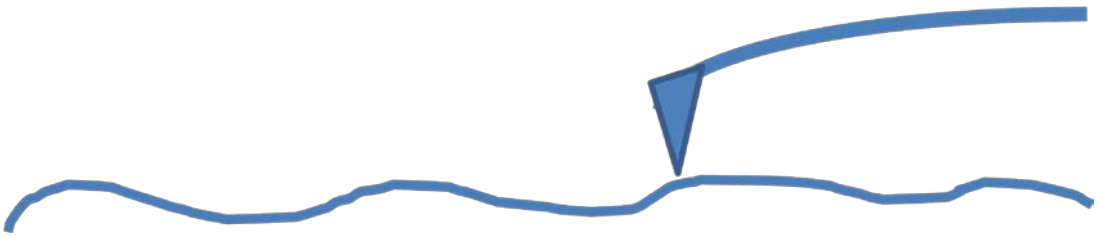

First scan in the tapping mode.

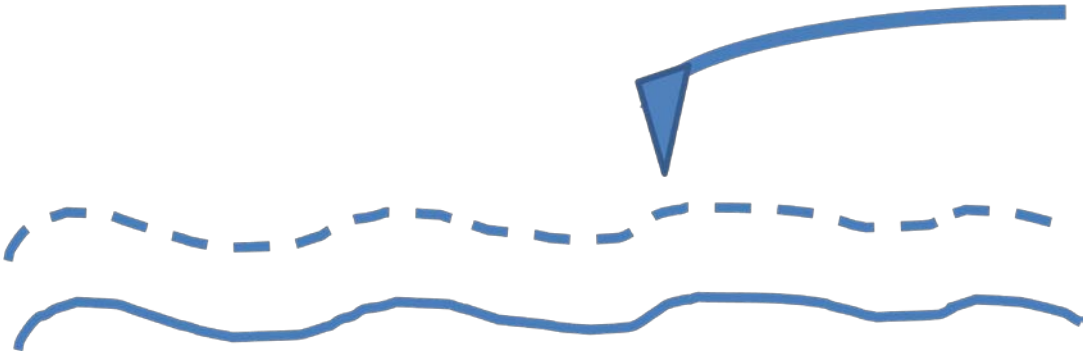

Second scan in the lift mode.

Fig. 27. The second scan is performed a predetermined distance above the sample surface that was mapped during the first scan. Thus, during the second scan the force measured is essentially due only to the longer range magnetic force.

In the second trace or the lift mode, the magnetic force gradient ($\partial f_z/\partial z$) comes into play. The oscillation of the magnetic tip can be described by a harmonic oscillator with an effective spring constant, $k_{eff} = k - \partial F_z/\partial z$. The modified spring constant produces the change in the natural resonance frequency of the cantilever ($f_n = \omega_n/2\pi$) :

$$f_n' = f_n \sqrt{1 - \frac{\partial F_z/\partial z}{k}}$$

$$\Delta f = f_n' - f_n \approx -\frac{f_n}{2k}\frac{\partial F_z}{\partial z}$$

where f_n is the natural resonance frequency of the cantilever without the magnetic force gradient and the positive z direction is chosen from the sample surface to the tip.

When the tip is attracted toward the sample, the force derivative is positive, resulting in a decrease in the resonance frequency of the cantilever (Fig. 28. (a)). The change in the resonant frequency can be detected by the change in the phase of its oscillation [77,78,79]. While the cantilever is being driven at a fixed frequency (f_n), the phase shift ($\Delta\varphi$) at the fixed drive frequency (f_n) is measured negative (Fig. 28. (b)). The opposite happens for a repulsive force: the increase in resonance frequency and phase shift (Fig.29). The sign of the phase shift thus provides an interpretation of the force: the positive shift for a repulsive force on the tip and the negative shift for an attractive force on the tip.

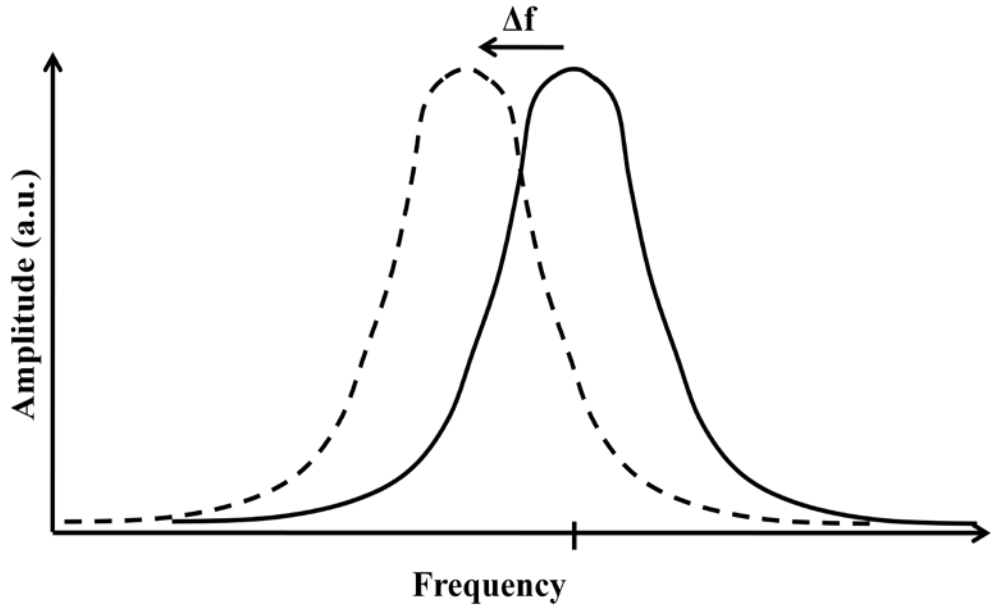

(a)

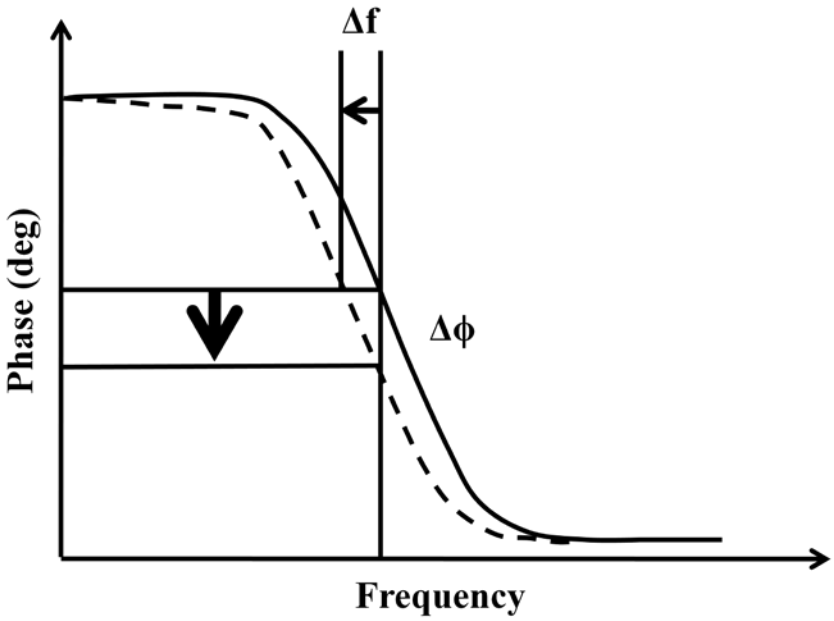

(b)

Fig. 28. An attractive force shifts the resonant frequency to a lower value, causing a negative phase shift to be measured at the drive frequency.

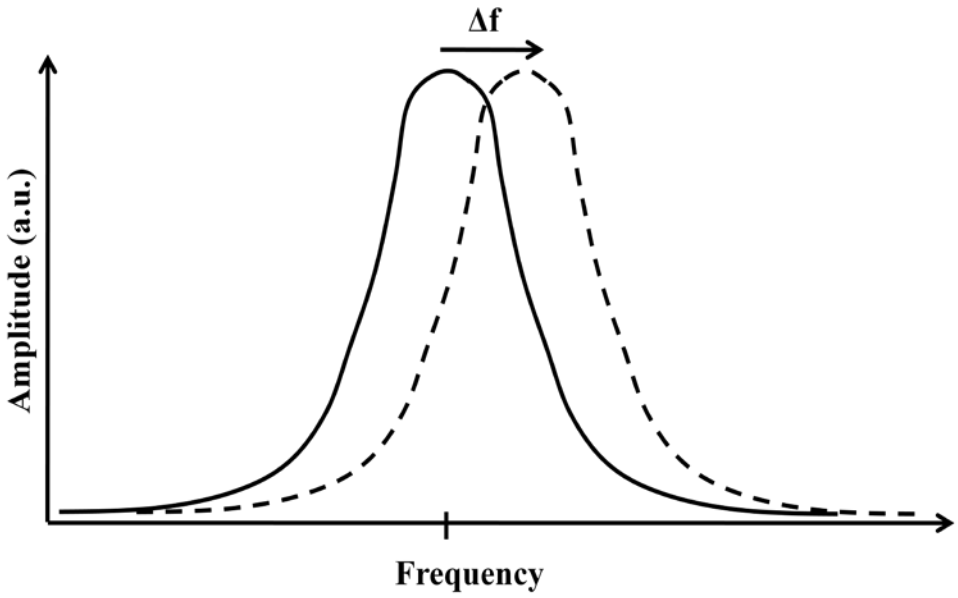

(a)

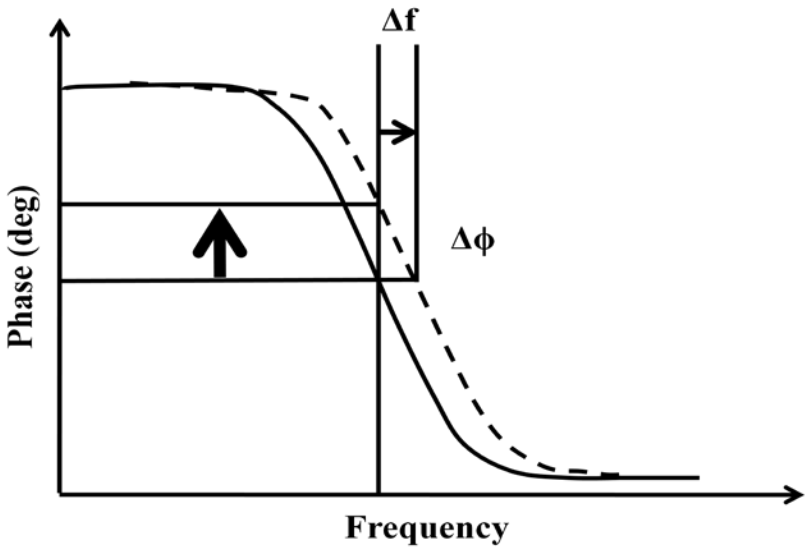

(b)

Fig. 29. A repulsive force shifts the resonant frequency to a higher value, causing a positive phase shift to be measured at the drive frequency.

Depending on the direction of the stray field from the sample with respect to the magnetization of the tip, the tip feels either an attractive or a repulsive force, changing the resonant frequency of the oscillation of the cantilever. If the directions of the magnetization of the tip and the stray field are parallel the tip feels an attractive magnetic force, reducing the resonance frequency. And as shown in Fig. 28, the negative change in the phase is detected and usually coded in black in the monitor of the MFM. Therefore, an attractive force gives the dark image and a repulsive force the light image in the screen of the MFM. This dark and light contrast makes it possible to estimate the magnetization of the surface below the tip, either out-of-plane or in-plane.

In the case where the magnetization of magnetic rods is out-of- plane, the tip senses one direction of the stray field due to each rod along the dotted line(Fig 30(a)). Therefore each magnetic rod with out-of-plane moment gives either a black image(attractive force) or a white image(repulsive force) on the MFM screen(Fig.30(a)). Each magnetic rod with an in-plane moment, however, gives a pair of black and white images. The stray field from each magnetic rod with a in-plane moment gives two directions at the dotted line (Fig.31(b)). Here all discussions assume that the tip is magnetized along the tip axis.

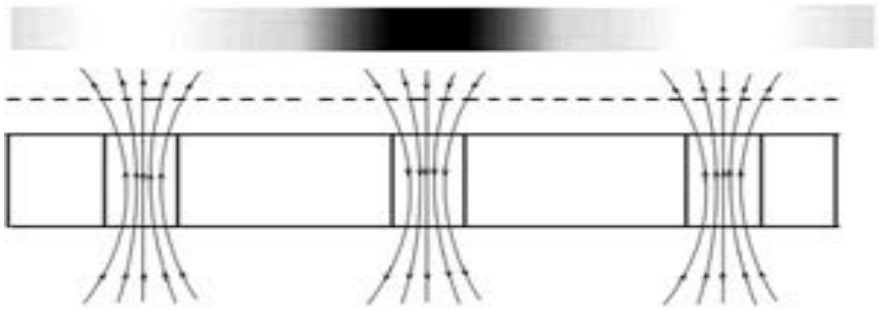

(a)

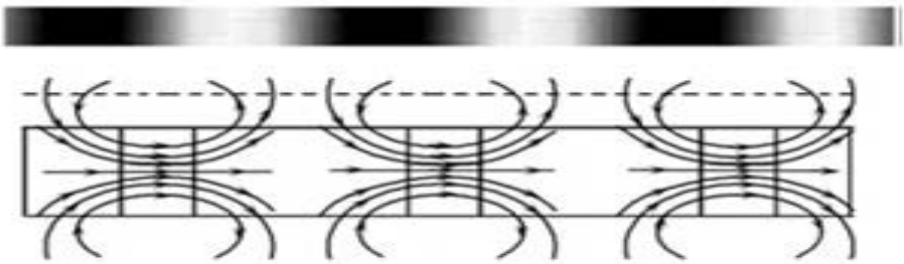

(b)

Fig. 30. Sketch of the stray field of magnetic dots and the MFM image with (a) an out-of-plane moment, and (b) an in-plane moment [80].

Fig.31 and Fig.32 show AFM/MFM images of Co nanowires with out-of–plane moments and in- plane moments, respectively. The Co nanowires with diameters of 65nm and 200nm were electroplated into a porous anodic aluminum oxide (AAO) membranes and then were polished to get a smooth surface for the MFM measurement. The panels on left of Fig.31. and Fig. 32. shows the AFM images: (a) the surface profile (b) topograhpic images and the MFM images (second scan) performed at a lift-up height or scan height of 30nm above the sample surface.

For Co nanowires with diameter of 65 nm, the MFM image of each nanowire is either dark or bright (Fig. 31 (c)). Therefore, according to the MFM interpretation, the 65nm diameter nanowires have out-of plane magnetic moments. In contrast to Fig. 31 (c), the MFM image of each nanowire with diameter of 200nm consists of a dark and a bright contrast spots(Fig.32 (c)). Therefore, the 200nm diameter nanowires have in-plane magnetic moments at the sample surface.

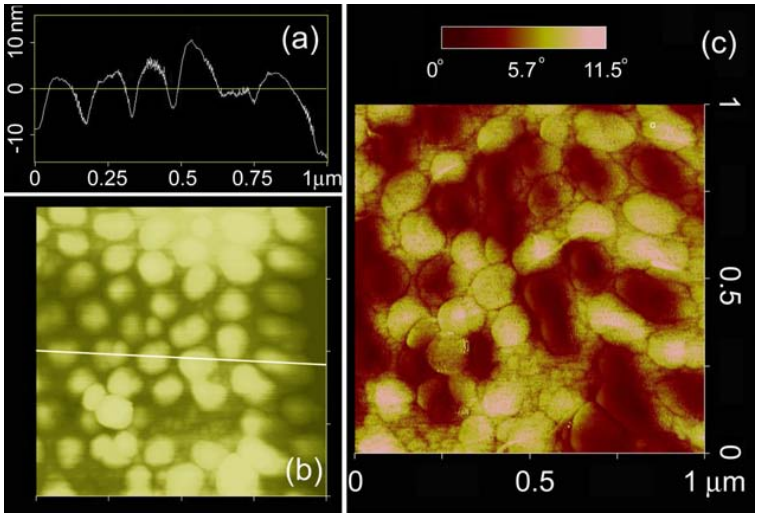

Fig.31. AFM ((a) and (b)) and MFM images of Co nanowires with a diameter 65nm[80].

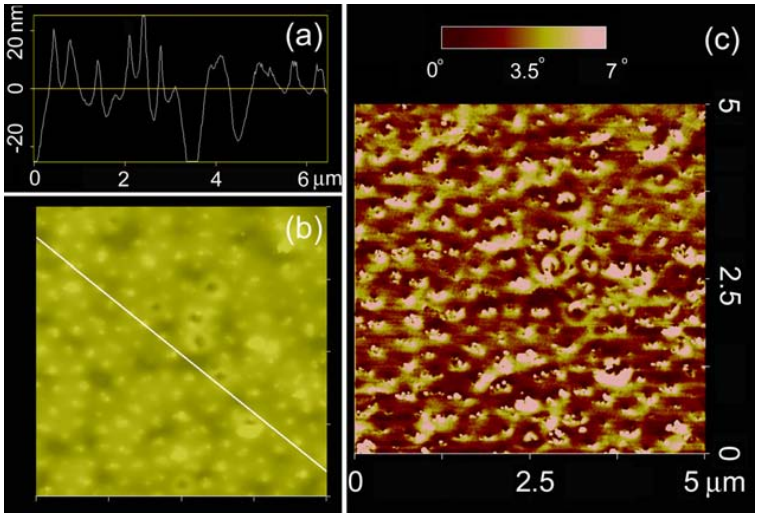

Fig.32. AFM ((a) and (b)) and MFM images of Co nanowires with a diameter 200nm[80].

Principles of Scanning Hall Probe Microscopy

Scanning Hall probe microscopy (SHPM) directly measures the magnetic field from the sample, as opposed to MFM which measures the field gradient [81, 82]. The direct image of magnetic field by SHPM allows for easier interpretation of the magnetization of the sample than MFM image does. However, because of the relatively lower resolution of the SHPM (about 500nm) than that of the MFM (about 50 nm), two magnetic imaging techniques complements each other.

During the scanning over the sample, a Hall probe images the magnetic field distribution by measuring the Hall voltage. The SHPM technique employs the scanning tunneling microscope (STM) or atomic force microscope (AFM) feedback to make the Hall sensor approach the sample surface and maintain the constant distance from the surface. The STM feedback, which was used in this study, uses the tunneling current between the STM tip and the sample surface in order to drive the feedback loop to maintain the constant tunneling current (Fig.33, 34). The STM tip is located near the corner of the chip (Fig. 33) and the chip is tilted about 1 or 2 degrees with respect to the sample surface to ensure the close proximity of the surface.

Because the STM feedback requires the conductive surface, the sample (Co nanorods in a PMMA matrix for this study) has to be coated with a thin layer of Au.

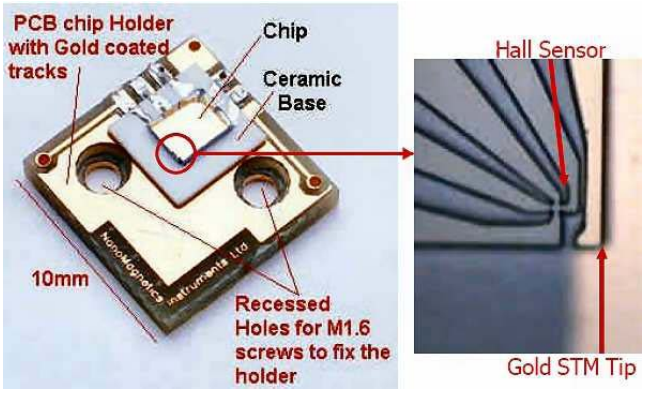

Fig. 33. A photograph of a hall probe chip.Courtesy of NanoMagnetics Instruments Inc. http://nanomagnetics-inst.com/

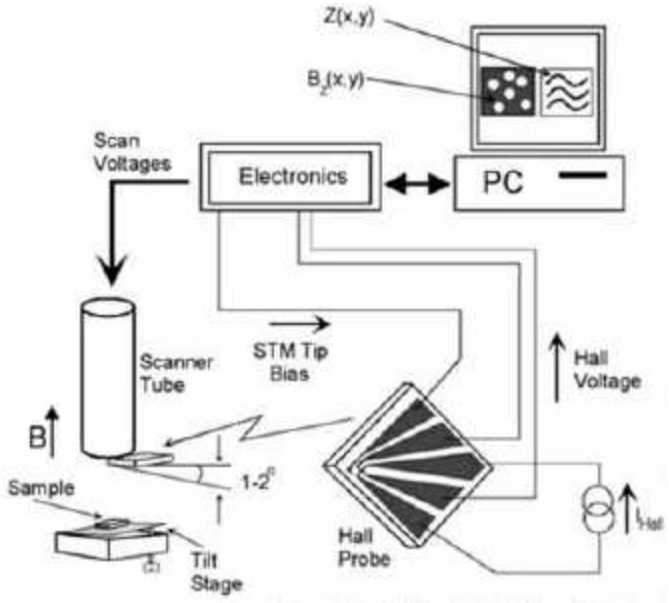

Fig. 34. Basic operation and components of SHPM. Courtesy of NanoMagnetics Instruments Inc. http://nanomagnetics-inst.com/

Magnetic Imaging of Co Nanorods by MFM and SHPM

This section explains the characterizaion of representative Co nanord used for this study. A Digital Instruments Nanoscope AFM/STM was used to characterize the mangetic structures for this dissertation. As expained in the previous chapter, the samples (cobalt nanorod in a PMMA matrix) were prepared by e-beam lithography and electroplating. For the MFM measurement, the PMMA was not removed to maintain the sample surface as flat as possible and thus minimize the influence of topography.

In order to measure the stray field from the magnetic structures, Scanning Hall Probe Microscopy (SHPM) was used to make a direct measurement of the stray field from the magnetic structures. Both MFM and SHPM images showed that the magnetic structures prepared were appropriate for this study of the hybrid systems; each nanorod stays in a single domain state (the out-of-plane magnetization) in zero field at room temperature and provides a strong magnetic field in the Tesla range at its top surface [35] . A schematic of the stray field pattern is shown in Fig.35.

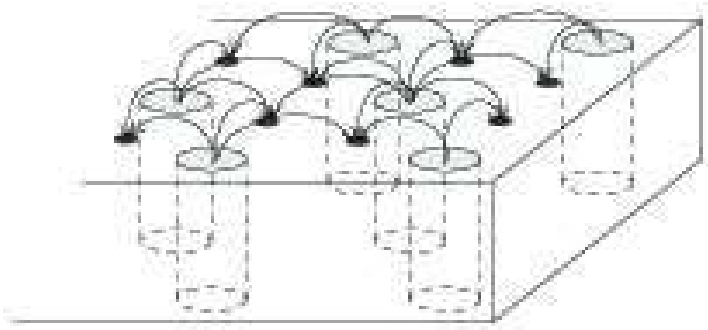

Fig. 35. Schematic magnetic field pattern on the surface of the MNR array.

Fig.36 shows the MFM image of the Co nanorods in the PMMA matrix and the profile of the phase shift along the scan line. The MFM measurement was performed at lift-up height or scan height of 30nm above the sample surface. The phase shift exhibits the different signs: the positive sign above the cobalt rod and the negative sign between the rods. The different signs correspond to the different direction of the normal component of the magnetic force or the stray field from the rod. As shown in Fig.30(a) and Fig.31, the one sign (positive) above the cobalt nanorod means that the nanorod has an out-of plane magnetic moment, which is desirable for this study of FSH.

MFM measurements at various lift-up heights showed that the magnetic interaction becomes weaker as the scan height increases (Fig.37).

In order to confirm the out-of –plane magnetic domain state, the SHPM measurement of the same array was performed at a scan height of 200nm above the surface (Fig.38). Imaging with SHPM was done by Dr.Ozmetin at Texas A&M University, Physics Department.

Bright and dark spots in the SHPM image correspond to the opposite direction of the magnetic field normal to the film: bright spot due to the magnetic field from the nano rod and dark spot due to the return field. From the one color (white) in the bright spot and the MFM image, it can be concluded that each nanorod has out-of-plane magnetic moments.

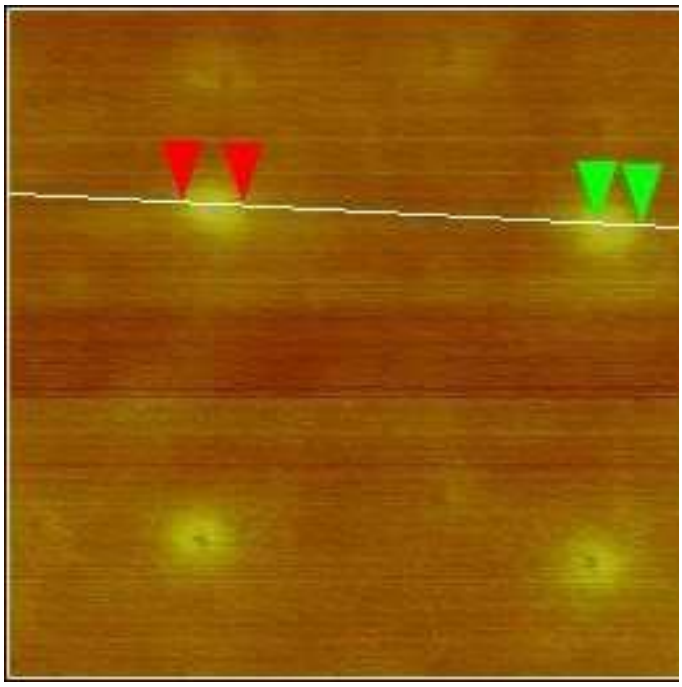

(a)

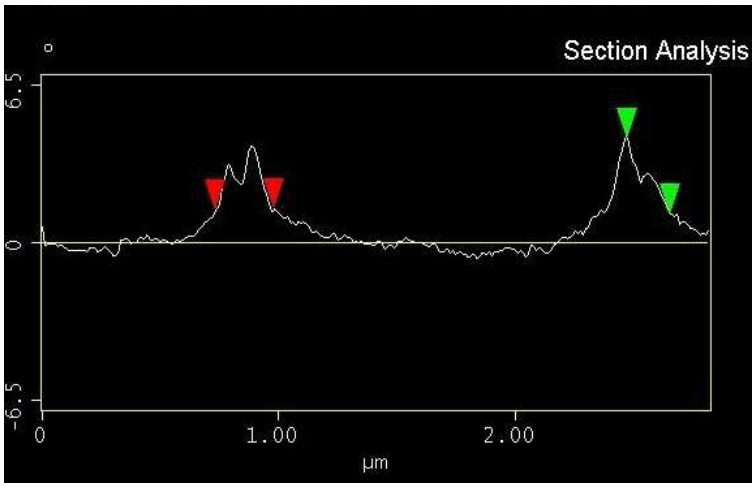

(b)

Fig. 36. (a) MFM image of Co nanorods in the PMMA matrix with a scan height 30 nm (b) a scan along the line marked in Fig.36 (a). The smaller positive phase shift above the center or the rod is due to the demagnetization of the magnetic rod.

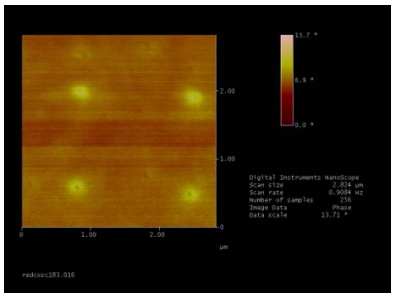

Lift-up height of 30 nm

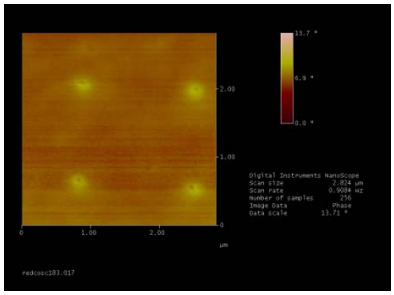

Lift-up height of 60nm

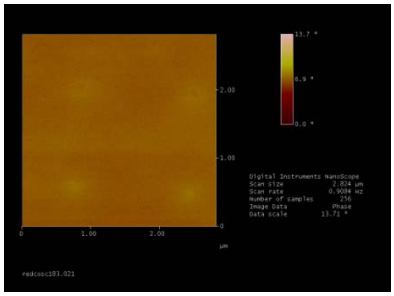

Lift-up height of 150 nm

Fig.37. The MFM images of the same array in Fig.36. With increased lift-up height, the contrast becomes weak.

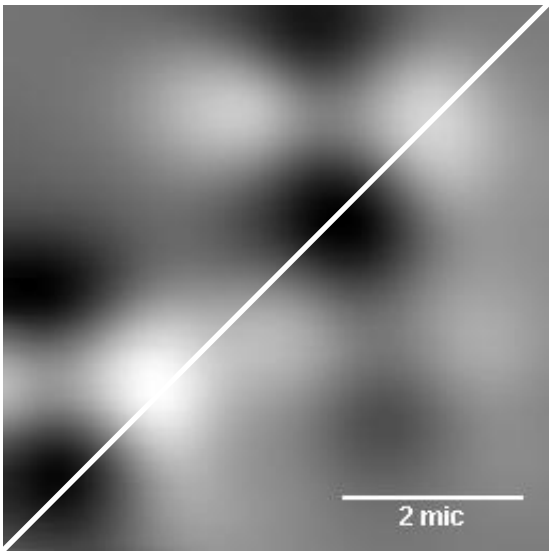

(a)

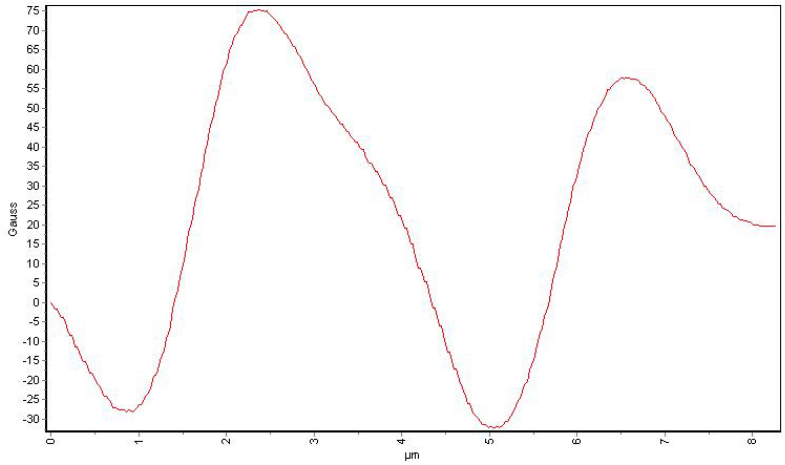

(b)

Fig. 38. (a) SHPM image of the alternating magnetic field distribution taken at 200nm above the surface of Co nanorods with a 2μm period. Bright and dark spots correspond to opposite directions of the magnetic field. (b) Profile of the magnetic field strength along the white line in Fig.38 (a).

CHAPTER IV
VORTEX PINNING BY A STRONGLY VARYING MAGNETIC FIELD (SVMF)

This chapter discusses the results of transport measurements on a superconducting film in an embedded FSH with a magnetic field that varies strongly (0 to $\pm$ 0.5 T) on the scale of the nanorod separation. The spatially alternating magnetic field was provided by Co magnetic nanorods with a high aspect ratio.

Vortex pinning in type II superconductors has been of both experimental and theoretical interest. Recent advances in nanotechnology such as electron beam lithography have made it possible to study the vortex in superconductors with controllable periodic pinning arrays. These artificially ordered non magnetic pinning arrays also have exhibited the effects of the commensurability between the periodic vortex lattice and the ordered pinning arrays. The artificial defect arrays also showed peak effects such as minima of the resistance and maxima of the critical current of a superconducting film when the vortex density was an integer multiple of the artificial defect density.

Recently, there has been a focus on the introduction of ferromagnetic materials as pinning centers. Besides the core pinning or structural effect, the FSH showed the more effective magnetic pinning of the vortices [81, 82]: the interaction between the vortex and the local magnetic fields of the magnetic structures.

Most FSH systems exhibited significantly increased critical current. The shift in the second critical field, however, is just in the militesla range with respect to a control superconducting system [81, 82].

This chapter reports that the embedded FSH system with magnetic nanorods showed four remarkable things:

1. enhancement in the critical current
2. enhancement in the second critical field
3.commesurabilty or matching effect
4. magnetism induced superconductivity or hysteric behavior of superconductivity.

In order to investigate how effectively Co MNRs enhance the superconductivity of Pb_{82} $Bi_{18,}$ both the embedded FSH and the control sample were prepared on a single substrate (Si/SiO_2). The embedded FSH consists of Co nanorods embedded in a 120nm thick film Pb_{82} Bi_{18} which was thermally deposited at liquid nitrogen temperature (Fig. 39). The thickness was chosen to make the superconducting film a type II superconductor. The control sample consists of the Pb_{82} Bi_{18} film only on Au. For comparison, the same thickness of Au was deposited for the control sample at the same time because the Au film was required as a cathode for electroplating Co in the embedded FSH. A Quantum Design model 6000 physical measurement system (PPMS) was used to make low temperature transport measurements.

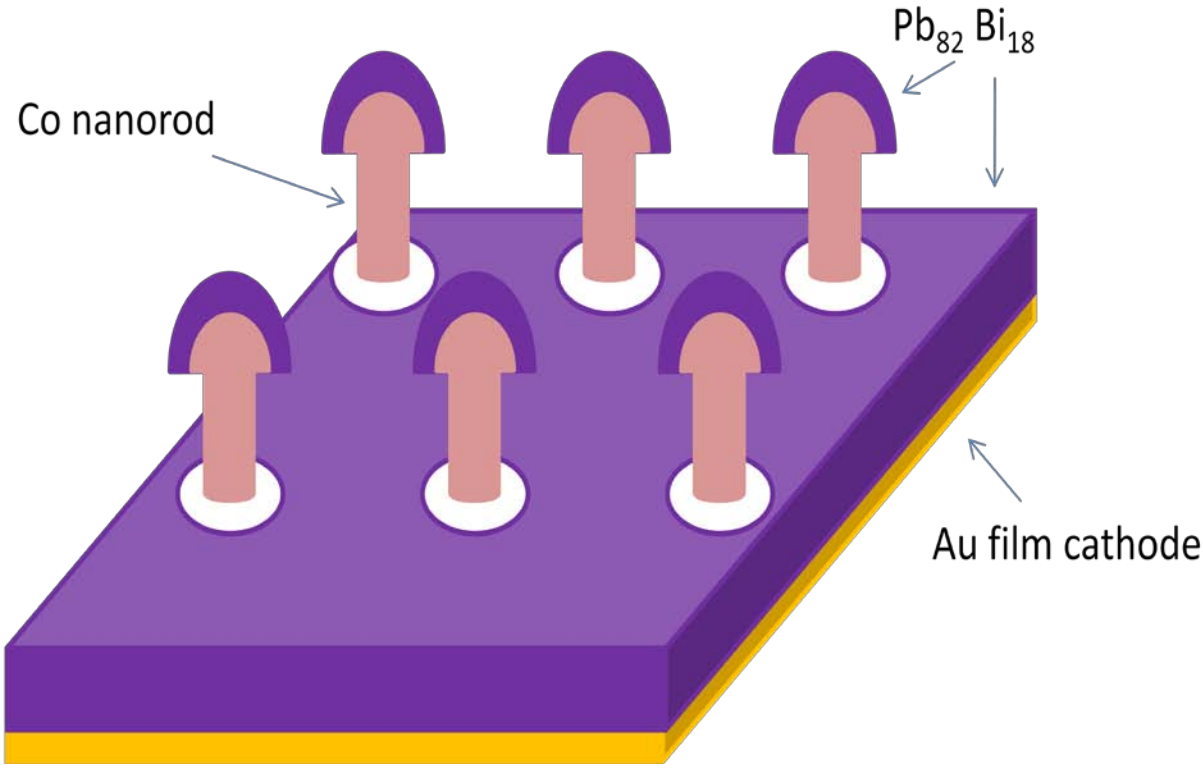

Fig.39. Schematic picture of an embedded FSH.

Critical Temperature and Critical Field

In order to determine the critical temperature T_c and the second critical field, H_{c2} of the superconducting film, DC transport measurements were performed. Above the second critical field, the superconducting film is in the normal and exhibits a finite electrical resistance.

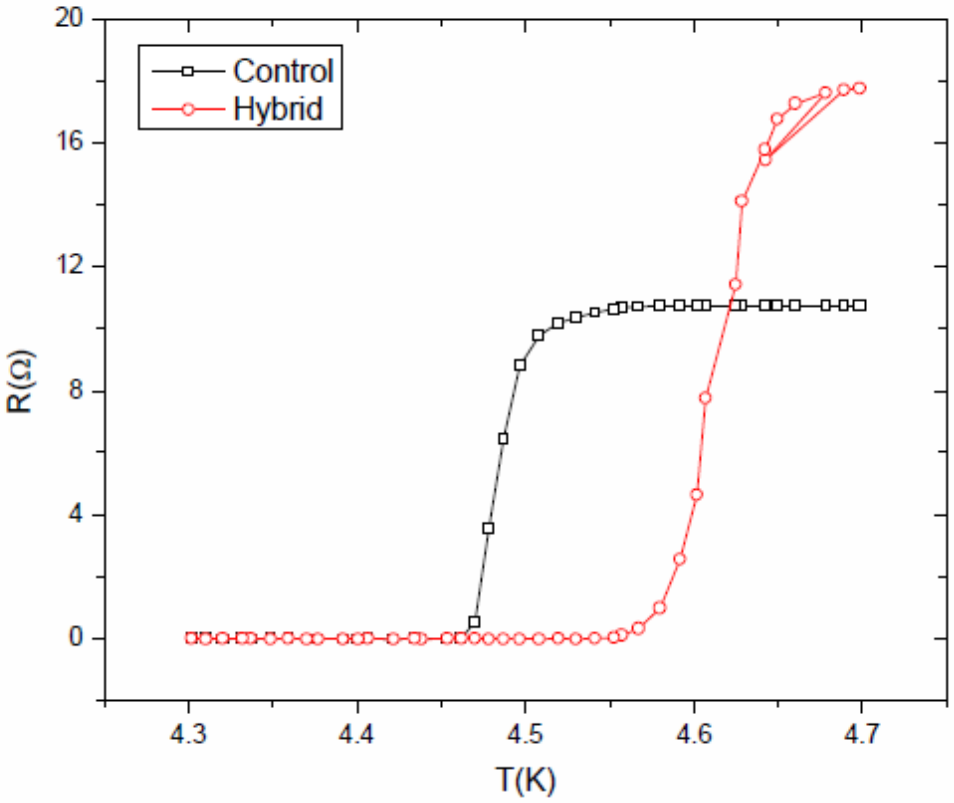

Fig. 40. T_c measurement of the control and FSH hybrid sample.

In Fig. 40 , the critical temperatures of both the FSH and control sample were reduced to about 4.55K and 4.45 K, repspectively,compared to the usual value of 7.8 K for a pure Pb_{82} Bi_{18} film. This was due to the well known proximity effect [2] between the superconducting film and the Au film which was deposited as a cathode for electrodeposition of Co nanorods. In order to confirm that this reduction in T_c was due to the proximity effect, two superconducting films were deposited at the same time on a single substrate: Pb_{82} Bi_{18} film on a Au film and Pb_{82} Bi_{18} film on Ag. While the critical temperature of Pb_{82} Bi_{18} film on Ag was not significantly affected by the proximity effect, that of the $Pb_{82}Bi_{18}$ film on Au film was lowered to about 4.5 K by the proximity effect.

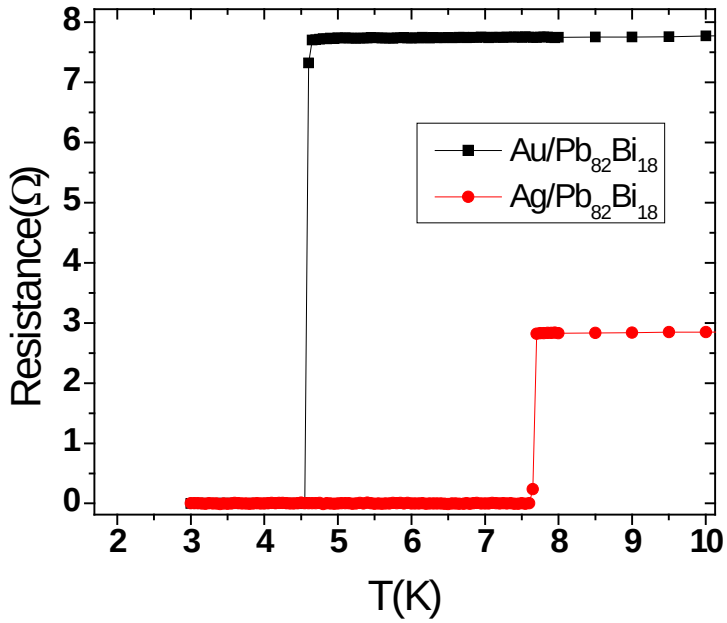

Fig. 41. Decrease in the critical temperature of Pb_{82} Bi_{18} film on Au film due to the proximity effect.

At a fixed temperature (4.45 K) where both samples are in the superconducting state, the magnetoresistance measurement was performed with magnetic field applied normal to the film. The resistance was measured at every 20 Oe from 0 to 3000 Oe with a sweeping rate 5 Oe/s. After 3000 Oe, the field increased up to 2T (20,000 Oe) with a sweeping rate 100 Oe/s and then remained at 2T for 300 seconds to ensure a full magnetization of the MNR in the embedded FSH and then reduced back to 3000 Oe.

In order to observe the hysteric behavior of FSH, from 3000 Oe through 0 Oe to –3000 Oe, the measurement was performed at every 20 Oe. After the measurement at – 3000 Oe, the field went to negative 2T to ensure a full magnetization in the opposite direction and then was reduced back to – 3000 Oe. Finally from – 3000 Oe to 0 Oe, the resistance was measured, completing one cycle of the field sweeping measurement. But, the cycle of the initial measurement included three more steps: the second magnetoresistance measurement from 0 Oe to 3000 Oe, full magnetization in the opposite direction up to - 2T and return to 0 Oe for the next field sweeping measurement at different temperatures. The second measurement from 0 Oe to 3000 Oe is different form the first measurement with the same range of the field because of the magnetization of MNR in the negative direction. Fig. 42 shows the cycle or the path of the magnetic field sweeps.

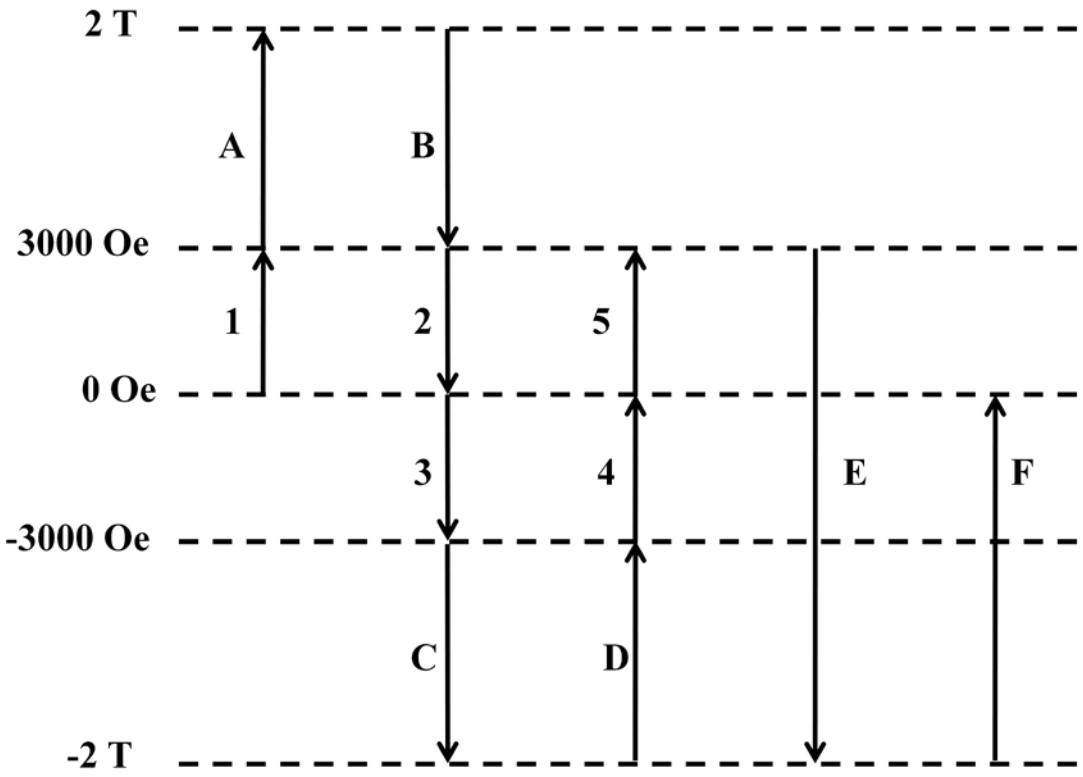

Fig. 42. Diagram of magnetic field sweeps. In this experiment, the applied magnetic field was always perpendicular to the film. During the steps 1 to 5, magnetoresistance measurement was performed. The field is swept up to 2T(step A) and – 2T (step B) in order to magnetize the Co nanorods. The step 5, E and F are only for the initial magnetoresistance measurements.

In Fig. 43, the upper critical field for the control sample (Pb_{82} Bi_{18} film on a Au film) is about 100 Oe. The magnetoresistance curve of the control sample depends only on the value of the magnetic field, not on the path of the applied magnetic field. Note that the small apparent hysteresis (about 20 Oe) shown in Fig.41 was demonstrated by calibration measurements of the field in the solenoid as a function of its current without a sample to be due to flux trapping in the solenoid. For all of the measurements, the field was determined by measurement of the magnet current rather than with a Hall probe. Thus, the small hysteresis plotted here is negligible to that due to the FSH sample.

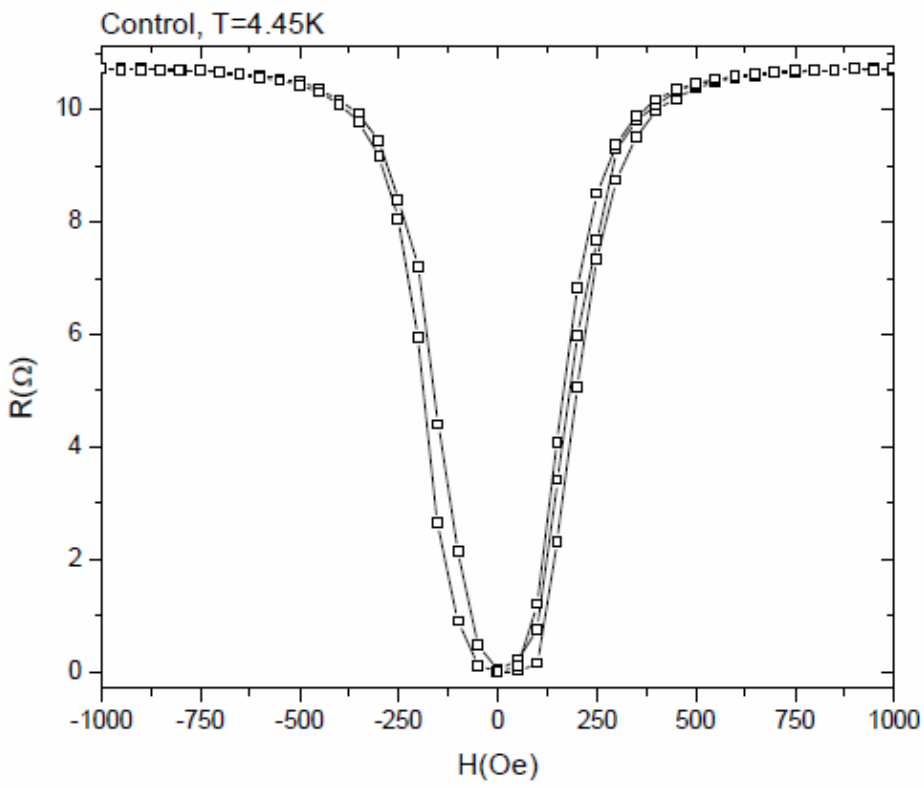

Fig. 43. R vs. H of the control at 4.45 K.

In contrast to the control sample, the hybrid or the FSH sample showed the hysteric behavior of the magnetoresistance due to hysteresis of the MNR: the resistance depends not only on the value of the applied magnetic field but also on the path or history of the magnetic field (Fig.44). The critical field H_{c2}, along the path 1 or from 0 Oe to 3000 Oe, is about 1000 Oe. After completion of a full magnetization of MNR up to a field of 2 T , the magnetoresistance was measured from 3000 Oe to 0 Oe along path 2 in Fig.44.

The critical field H_{c2}, along path 2, is remarkably increased to about 1300 Oe ,compared to the upper critical field (100 Oe)of the control sample. Also the critical field along the path 2 differs from that along the path 1 by about 300 Oe.

The critical field H_{c2} ,along path 3 or from 0 Oe to – 3000 Oe, is about - 700 Oe. Similarly in the positve applied field, the field was swept to – 2 T to ensure the full magnetization in the opposite direction. The critical field H_{c2} ,along path 4 or from – 3000 Oe to 0 Oe, is about – 1300 Oe. The discrepency between along path 3 and 4 is about 600 Oe.

Finally, the critcal field H_{c2} ,along path 5 from 0 Oe to 3000 Oe, is about 700 Oe. The critical fields along path 1 and path 5 differ by 300 Oe. The difference comes from the different history of the magnetization process: while the MNRs are magnetized from the initial magnetization along path 1, the MNR are magnetized from the opposite direction along path 4 and 5. The critical fields along the path 2 and 4 are symmetric as are the critical fields along the path 3 and 5 (Fig. 44).

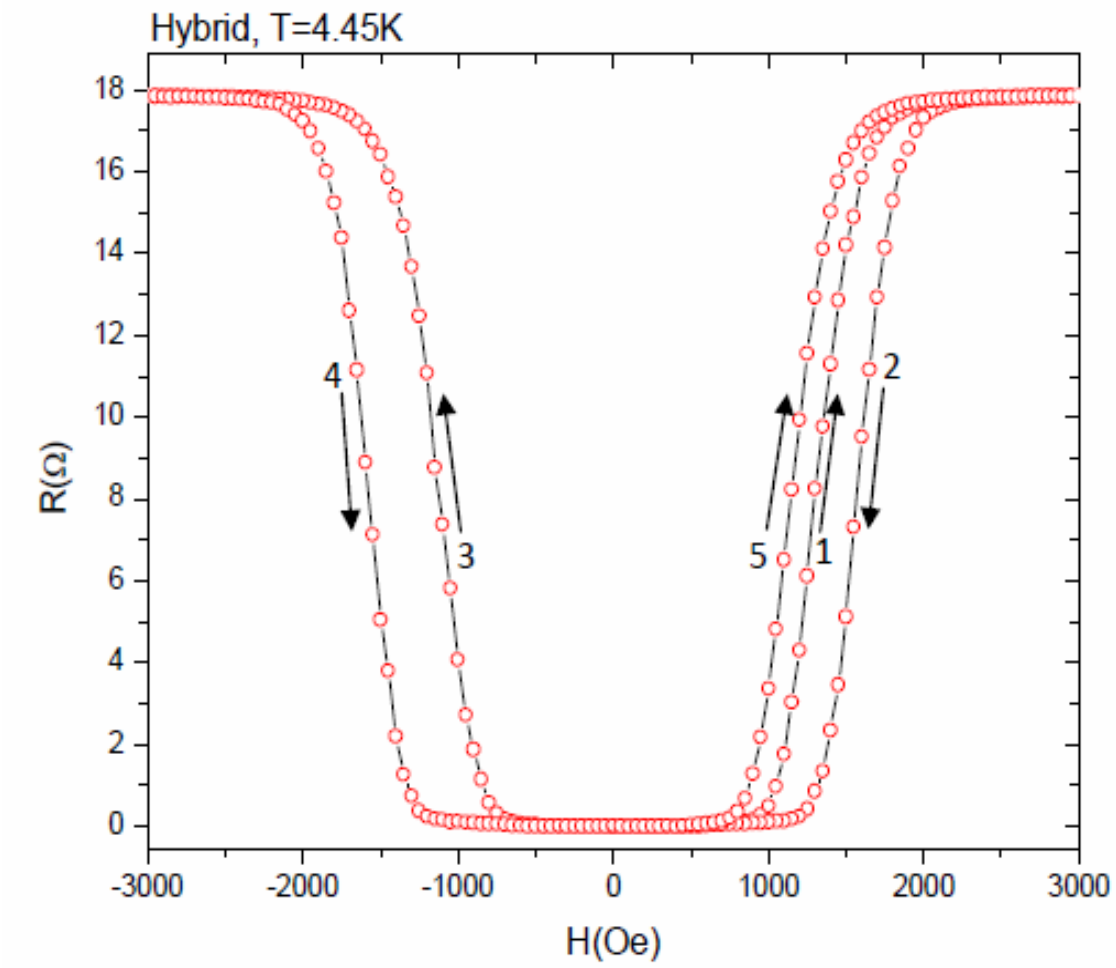

Fig. 44. Hysteric behavior of the magentroresistance of the hybrid or FSH sample. Arrows indicate direction of field sweep.

In the magentoresitance meaurement, the embedded FSH sytem exhibited two remarkable phenomena : the large enhancement in the upper critical field and the hysteric behavior of the magnetoresistamce (Fig.44).

This enhancement in the upper critical field is explained by the compensation effect. The magnetic stray field from the MNR forms the dipole loops (Fig.10). The field emanating from the rods changes direction between the rods. The stray field pointing downward between the rods effectively cancels the externally applied magnetic field. As a result, the embedded FSH can remain superconducting, at least in part of the film, in a higher external magnetic field (1300 Oe along path 2 in Fig. 44) than the control sample can.

Consider the magnetoresistance value at 1000 Oe along the paths 2 and 5 in Fig.44. The same value of the magnetic field 1000 Oe gives different values of resistance. At 1000 Oe along path 2, the film is still in the superconducting state. This means that the stray field which points downward between the rods can cancel the external magnetic field which points upward. However, at the same magnetic field along path 5, superconductivity is already destroyed, which means the stray field between the rods cannot fully compensate the external field. Therefore, the superconductivity in the embedded FSH depends not only on the field value itself, but also the history of the applied magnetic field. This hysteric behavior of the magnetoresistance comes from the magnetic hysteresis of Co nanorods. Also the different magnetoresistance value up to about 2000 Oe implies that at least more than 2000 Oe is needed to fully magnetize the Co rods in the sample.

Field Matching Effect

After the measurement along path 5 in Fig.44, the magnetic field was swept to – 2 T and held for 300 s at that field value and finally returned to 0 Oe to make the next field-sweep measurement at five different temperatures near $T_{C.}$ The field sweep follows the same way as in the previous magnetoresistance measurement at 4.45 K except the final three steps shown in Fig.42. The magnetoresistance of the control sample at different temperatures in Fig.45 shows the behavior of an ordinary superconductor. As the field increases, the resistance value monotonically increases.

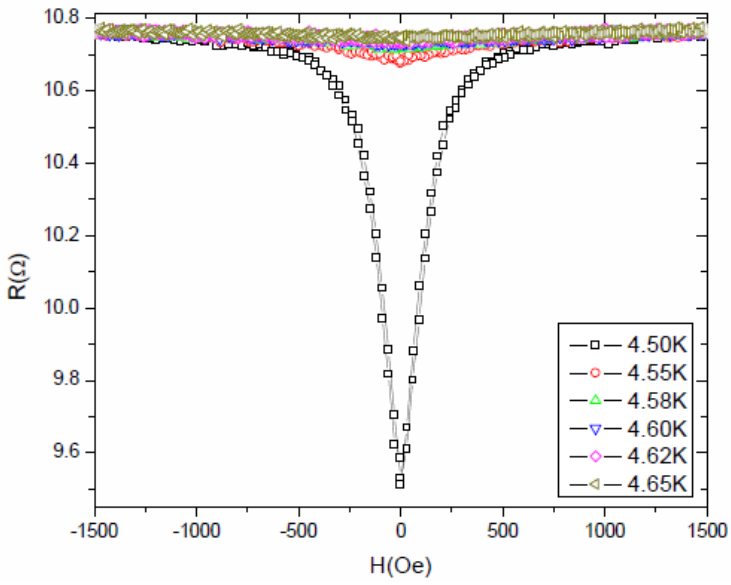

Fig. 45. R vs. H of the control sample at various tempratures near T_c, respectively.

In contrast to the control sample, the hybrid or the FSH sample exhibits the field matching effect near the crtical temperaure and its hysteric behavior. A sudden decrease in the resistance was observed at the specific field values , about 270, 540 and 810 Oe (a sharp change in slope rather than minimum) (Fig.46). The degree of decrease in the resistance at the fields as well as the resistance value showed hysteric behavior. The decrease in the resistance is more evident when the external magnetic field was swept from the saturation field (+ 2 T or – 2T) to zero field.

As the external magnetic field increases, the number of vortices increases. The field matching effect takes place when the number of vortices in the unit cell of the artificial array becomes an integer multiple. At the matching fields, the vortex pinning is greatly enhanced, resulting in a decrease in the resitance and an increase in the critical current.

The theoretical matching field for this triangular array is $H_1 = \frac{\Phi_0}{A}$ = 270 Oe.

Here $\Phi_0 = \frac{h}{2e} = 2.06 \times 10^{-15}\ Wb$ and A is the area of the unit cell in the triangular lattice with a lattice constant 300 nm. The agreement of the matching field in theoretical and experimental value results from the high degree of ordering in the Co nanorod array.

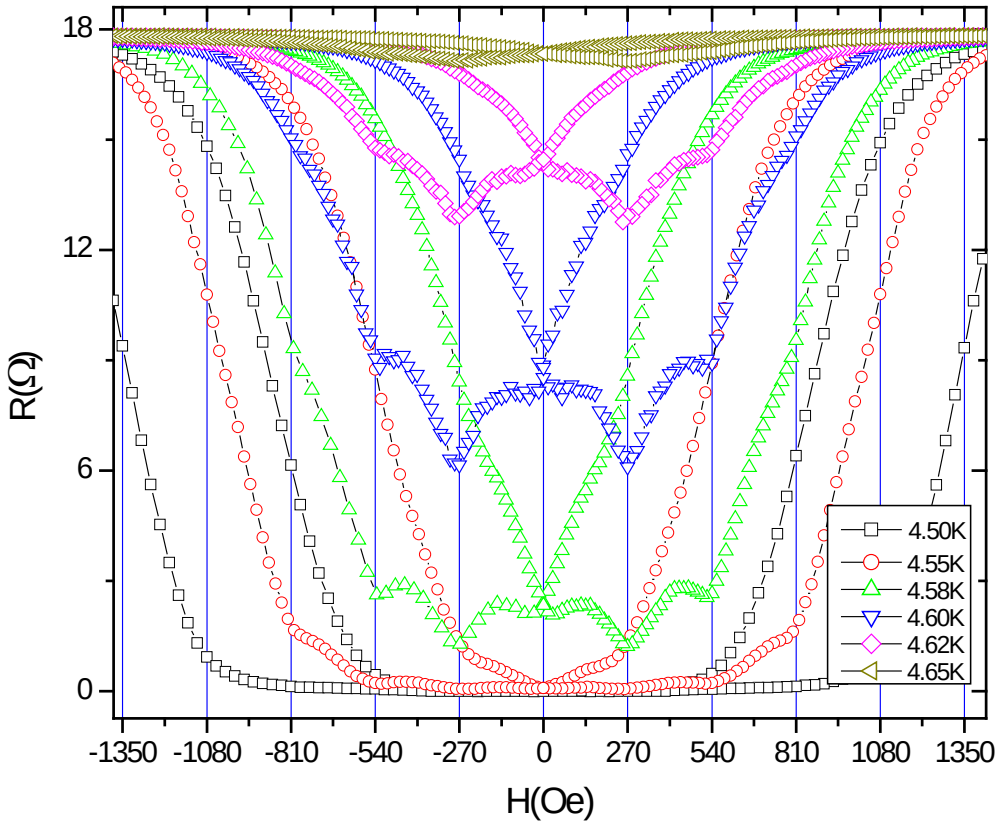

Fig. 46. R vs. H of the hybrid sample at various tempratures near T_c, respectively.

Magnetroresistance measurements well below the critical temperaure did not show the matching effect (Fig. 47). The superconductivity well below the critical temperarure is more stable than near the critical temperature under the relatively higher magnetic field. Well below the critical temperature, superconductivity is not so dependent on the external magnetic field as near the critical temperature. These measurements, however, do permit the determination of the phase diagram, $H_c(T)$, for these two samples.

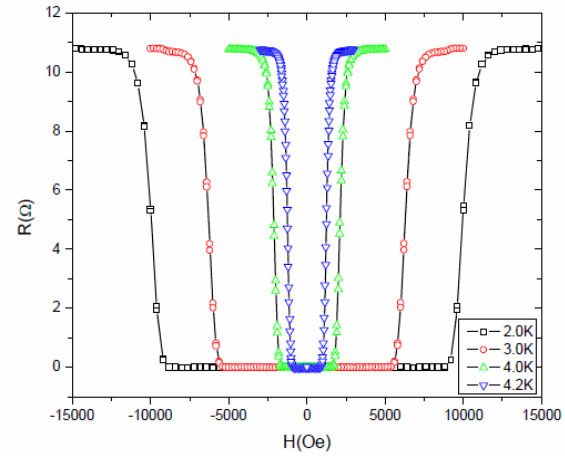

(a)

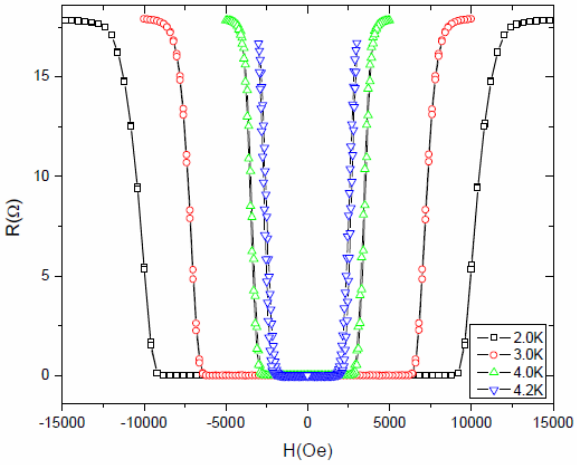

(b)

Fig.47. (a) and (b) R vs. H of the control and hybrid sample well below T_c, respectively.

Phase Diagram

In order to obtain the H-T phase diagram of the superconducting films, the resistance was measured as a function of temperature at various magnetic field values.
The critical temperature for each applied magnetic field was defined by extrapolation of each resistance curve to zero. The measurement was performed from 0 Oe to 3500 Oe , from 3500 Oe to 0 Oe, from -100 Oe to – 3500 Oe , and finally -3500 Oe to 0 Oe. The interval of the magnetic field was 100 Oe. The temperature was swept from above T_C to below T_C (Figs.48-51).

For the control sample, as the magnetic field increases, the critical temperature monotonically decreases. While the critical temperature of the control sample depends only on the field value, the critical temperature of the hybrid or FSH sample depends not only on the field, but also the history of the magnetic field. When the field was swept from the saturation field to a certain field value, the critical temperature is higher than when the field was swept from the opposite direction to the field value. This increase in the critical temperature is due to the fact that the internal field from the cobalt nanorods effectively cancels the external magnetic field. Fig. 52 shows the phase diagram of the hybrid or FSH sample. The maximum critical temperature around $\pm$ 300 Oe shows that the most effective compensation effect takes place around those field values in the sample. The butterfly like shape of the phase diagram comes from the hysteresis of the Co rods magnetization. The T_C (H) modulation near T_C , shown in Fig. 52 (b) , can be explained by Little Parks effect [83]. According to Little Pakrs effect, the resistance minima and critical current maxima at the matching field originate form the T_C suppression at the non-matching field.

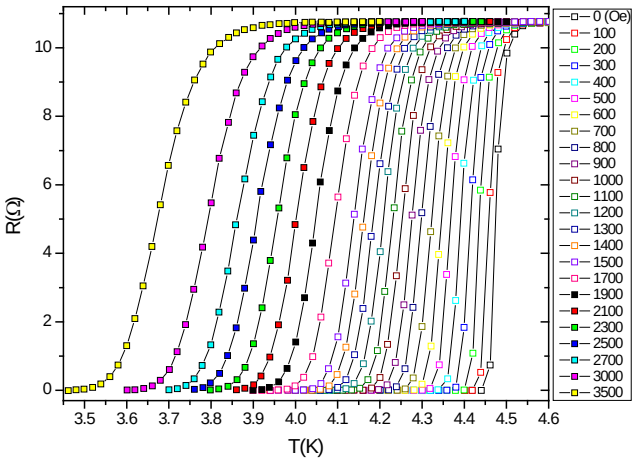

(a)

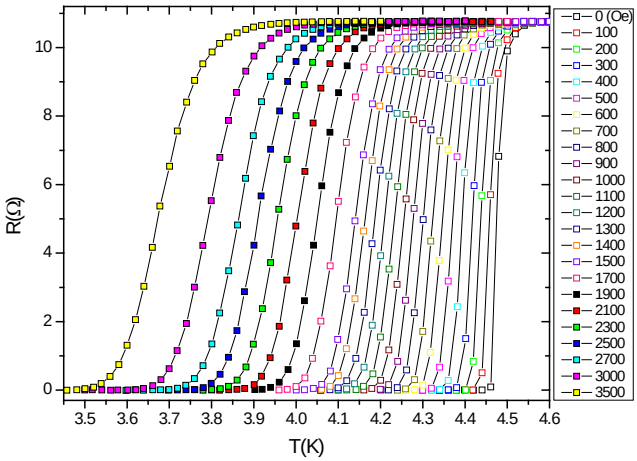

(b)

Fig. 48. R vs. T of the control sample.

(a): R(T) from 0 Oe to 3500 Oe

(b): R(T) from 3500 Oe to 0 Oe.

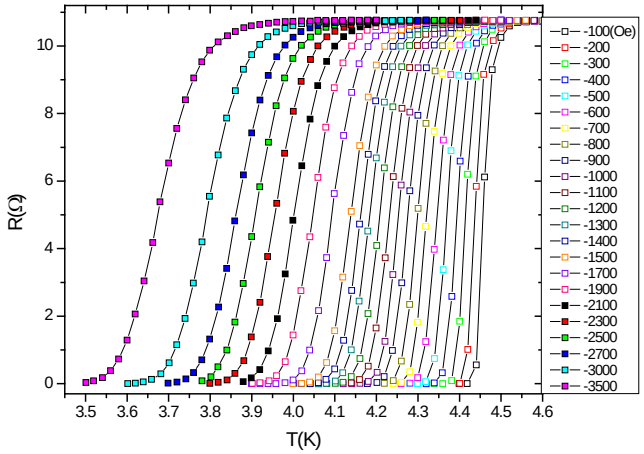

(a)

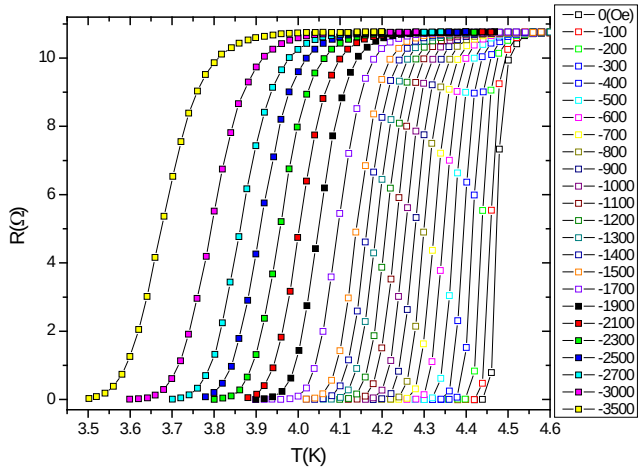

(b)

Fig. 49. R vs. T of the control sample.

(a): R(T) from -100 Oe to -3500 Oe

(b): R(T) from -3500 Oe to 0 Oe.

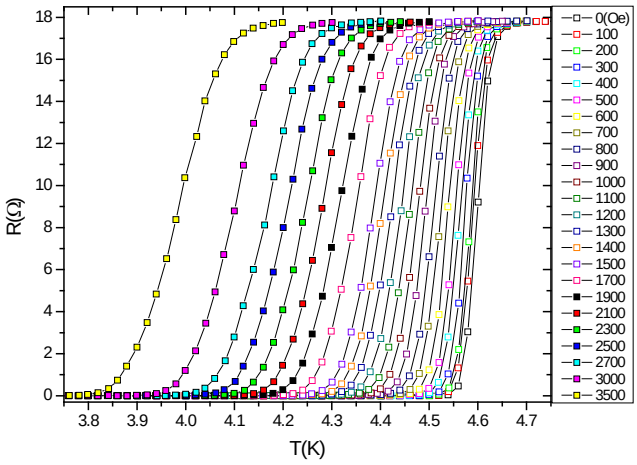

(a)

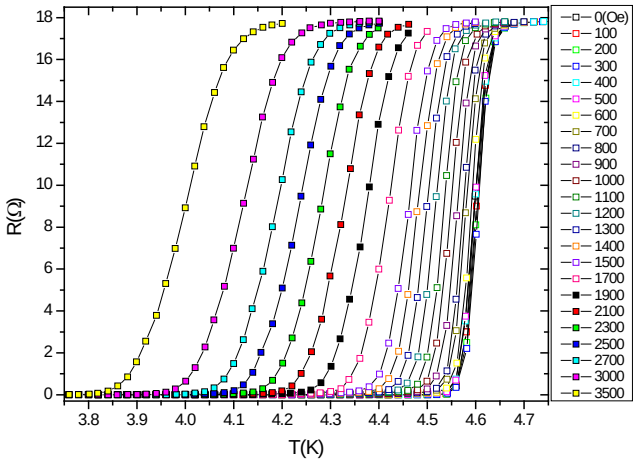

(b)

Fig. 50. R vs. T of the hybrid sample.

(a): R(T) from 0 Oe to 3500 Oe

(b): R(T) from 3500 Oe to 0 Oe.

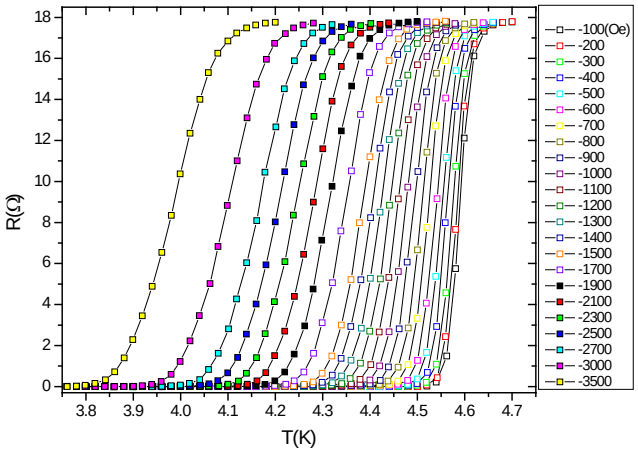

(a)

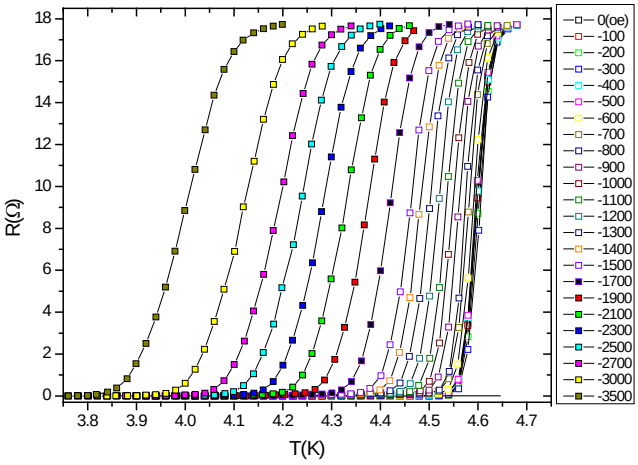

(b)

Fig. 51. R vs. T of the hybrid sample.

(a): R(T) from -100 Oe to -3500 Oe

(b): R(T) from -3500 Oe to 0 Oe.

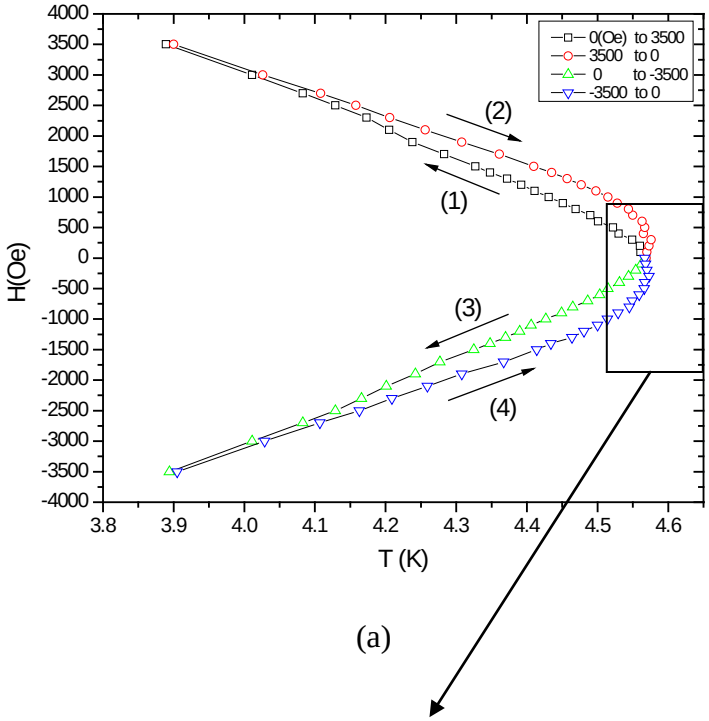

(a)

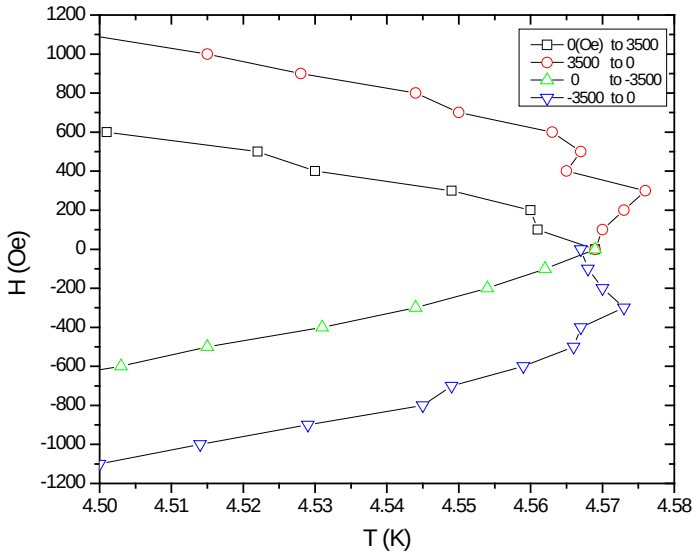

(b)

Fig. 52. (a)The phase diagram of the hybrid sample;(b) an expanded scale near T_c.

Critical Current Measurement

Critical measurements (I_C) were performed with a standard AC four probe technique in the PPMS. The current value at which a voltage of 2 μV is induced across the sample was chosen as I_C. Compared to the critical current of the control sample, the critical current in the hybrid sample was enhanced in a wider range of the temperature (all temperatures below T_C) and magnetic field (except very small fields) (Fig. 53).

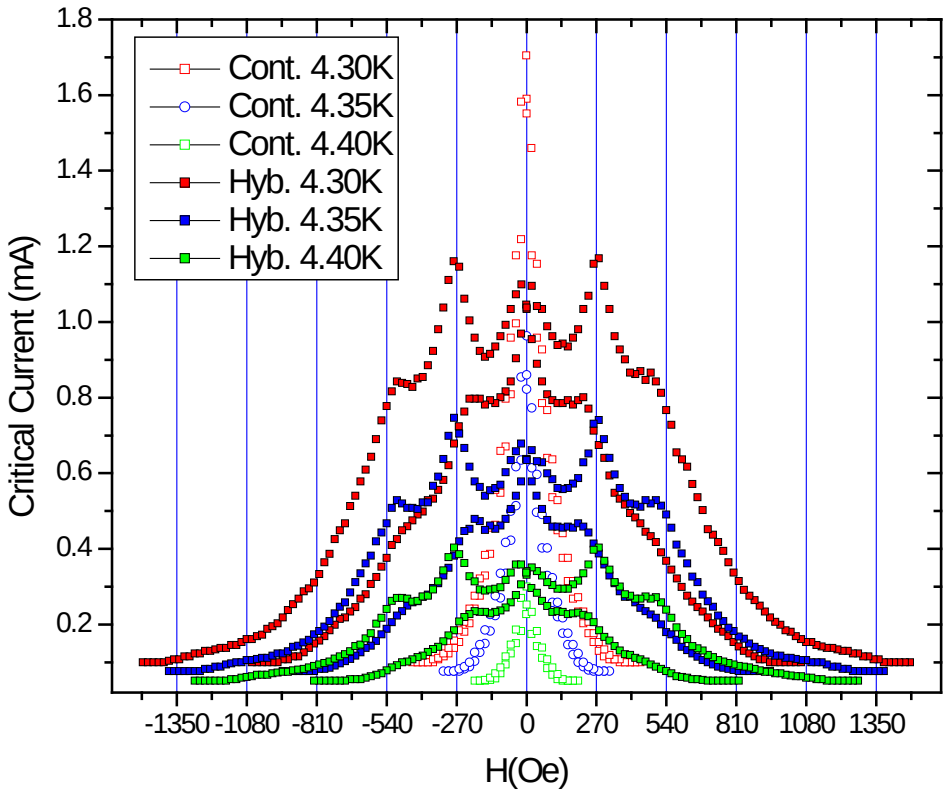

Fig. 53. Critical current vs. H of the control and hybrid sample.

The enhancement in the critical current provides clear evidence that the Co nanorods can effectively pin vortices in the hybrid or FSH system. In contrast to the control sample, the hybrid sample shows a matching field effect and hysteric behavior of the critical current. Sharp increases in the critical current of the hybrid sample are observed at the specific field values, about 270 Oe and 540 Oe (Fig. 53). The matching effect in the critical current measurement and the resistance measurement discussed in the previous section confirm that the array of the Co nanorods is highly ordered.

The critical current of the hybrid sample depends not only on the applied magnetic field but also on the history of the magnetic field. As shown in Fig. 54, the critical current along path 2 and 4 are higher than along path 1 and 3, respectively. This overall increase (path 2 and 4) is due to the field compensation effect. When the magnetization of more Co rods are parallel to the external magnetic field (path 2 and path 4), the stray field between the rods is anti-parallel to the external field, reducing the net magnetic field felt by the superconducting film.

Along path 1 and 3, the critical current decreases up to the first matching field and does not show such a strong second matching effect as along path 2 and 4, respectively. Along path 2 and 4, or while the field is ramped down from the saturation field, the critical current shows the stronger first and second matching effect than along path 1. This more pronounced matching effect along path 2 and 4 is due to the stronger magnetization of the Co nanorods. Both the overall increase and more pronounced matching effect (along path 2 and 4) confirmed that the vortex pinning in the embedded FSH comes mainly from the magnetic contribution, rather than a structural contribution.

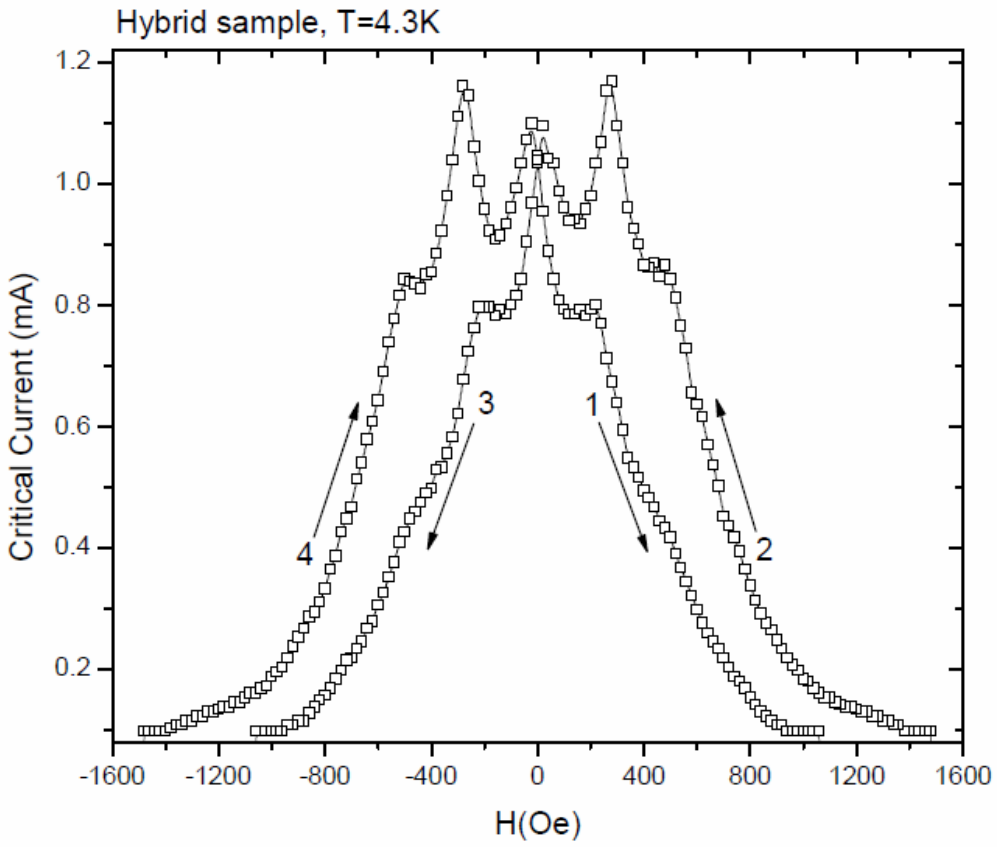

Fig. 54. Critical current vs. H of the hybrid sample at 4.3 K.

CHAPTER V

CONCLUSION AND FUTURE WORK

A strongly varying magnetic field (SVMF) was proved to effectively pin the vortices in the Ferromagnet-Superconductor Hybrids (FSH). The SVMF was created by a triangular array of magnetic nanostructures with a high aspect ratio. The cobalt magnetic nanorods with a 100 nm diameter and 300 nm height were successfully fabricated by electron beam lithography and electroplating method. The cobalt nanorods were arrayed to form a triangular lattice with a 300nm spacing, which resembles the natural array of the superconducting vortices. The magnetic force microscopy (MFM) and scanning Hall probe microscopy (SHPM) were used to characterize the magnetic properties of the nanorods.

The transport measurement of the embedded FSH exhibited enhancements in the critical current and the second critical field of a superconducting film (Pb_{82} Bi_{18}). Especially, the increase in the critical temperature over a wide range of the temperature and external magnetic field is critical in the application of superconducting materials. Also the embedded FSH showed the field compensation effect, matching effect and magnetism induced superconductivity.

In order to fully understand the dynamic interaction between magnetic nanorods and vortices and between vortices, the FSH has to be investigated by the low temperature MFM and SHPM. The direct observation of vortices will help understand the mechanism of vortex pinning in the FSH systems.

In order to decide whether the Little Parks effect accounts for the oscillation of the critical temperature in the phase diagram, more magnetoresistance measurements will be needed.

The transport measurement of embedded FSH with other magnetic materials such as Fe and Ni can be performed to find a method where magnetic information such as hysteresis can be extracted from the transport measurement.

For future applications, the study of the embedded FSH can be extended to the high T_C superconductors such as YBCO (Yttrium barium copper oxide).

REFERENCES

[1] P.G. De Gennes, Superconductivity of Metals and Alloys, W.A. Benjamin, New York, (1966).

[2] J.B. Ketterson, S.N. Song, Superconductivity, Cambridge University Press, Cambridge, New York (1999).

[3] V. Jeudy , C. Gourdon, Phys. Rev. Lett. 92 (2004) 147001.

[4] U.Essmann, H. Trauble, Phys.Lett.24A (1967) 526.

[5] G. Blatter, M.V. Feigelman , V.B. Geshkenbein , A.I. Larkin , V.M. Vinokur, Rev. of Mod. Phys. 66 (1994) 1125.

[6] I.F. Lyuksyutov, V.L. Pokrovsky, Adv. in Phys. 54 (2005) 67.

[7] M. Baert, V.V. Metlushko, R. Jonckheere, V.V. Moshchalkov, Y. Bruynseraede, Phys. Rev. Lett. 74 (1995) 3269.

[8] A.T. Fiory, A.F. Hebard, and S. Somekh, Appl. Phys. Lett. 32 (1978) 73.

[9] A.F. Hebard, A.T. Fiory, and S. Somekh, IEEE Trans. Magn. 1 (1977) 589.

[10] V.V. Moshchalkov, M. Baert, V.V. Metlushko, E. Rosseel, M.J.Van Bael, K. Temst, R. Jonckheere, Y. Bruynseraede, Phys.Rev. B 54 (1996) 7385.

[11] V.V. Moshchalkov, M. Baert, V.V. Metlushko, E. Rosseel, M.J.Van Bael, K. Temst, Y.Bruynseraede, R. Jonckheere, Phys.Rev. B 57 (1998) 3615.

[12] A. Castellanos, R. Woerdenweber, G. Ockenfuss, A. V.D. Hart, K. Keck, Appl. Phys. Lett. 71 (1997) 962.

[13] M. Baert, V.V. Metlushko, E. Rosseel, V.V. Moshchalkov, and Y. Bruynseraede, Europhys. Lett. 29 (1995) 157.

[14] V.V. Metlushko, U. Welp, G.W. Crabtree, Zhao Zhang, S.R.J.Brueck, B. Watkins, L.E. DeLong, B. Ilic, K. Chung, P.J.Hesketh, Phys. Rev. B 59 (1999) 603.

[15] A. I. Larkin and Y. N. Ovchinnikov, J. Low Temp. Phys. 34 (1979) 409.

[16] L. Civale, A. D. Marwick, T. K. Worthington, M. A. Kirk, J. R. Thompson, L. Krusin-Elbaum, Y. Sum, J. R. Clem,F. Holtzberg, Phys. Rev. Lett. 67 (1991) 648.

[17] A. I. Bazdin, Phys. Rev. B 47 (1993) 11416

[18] I.F. Lyuksyutov, D.G.Naugle, Modern Phys.Lett.B 13 (1999) 491.

[19] I.F. Lyuksyutov, D.G.Naugle, Intern.J.Mod. Phys. B 17 (2003) 3713.

[20] Y. Nozaki, Y. Otani, K. Runge, H. Miyajima, B. Pannetier, J. P. Nozières, G. Fillion, J. Phys. 79 (1996) 8571.

[21] D.J. Morgan , J.B. Ketterson, Phys. Rev. Lett. 80 (1998) 3614.

[22] Y.Otani, J.P. Nozieres, D. Givord, J.Magn.Mag.Mat., 126 (1993) 622

[23] O. Geoffroy, D. Givord,, Y.Otani B Pannetier F.Ossart, J.Magn.Mag.Mat., 121 (1993) 223

[24] M.J. Van Bael, K. Temst, V.V. Moshchalkov, Y. Bruynseraede, Phys. Rev. B 59 (1999) 14674.

[25] M.J. Van Bael, L. Van Look, K. Temst, M. Lange, J. Bekaert, U.May, G.Guntherodt, V.V. Moshchalkov, Y. Bruynseraede, Physica C 332 (2000) 12.

[26] M.J. Van Bael, J. Bekaert, K. Temst, L. Van Look, V.V. Moshchalkov, Y. Bruynseraede, G.D. Howells, A.N. Grigorenko, S.J.Bending, G. Borghs, Phys. Rev. Lett. 86 (2001) 155.

[27] M.V. Milosevic, S.V. Yampolskii, F.M. Peeters, Phys. Rev. B66

(2002) 024515.

[28] I.K. Marmorkos, A. Matulis, F.F. Peeters, Phys.Rev.B 53 (1996) 2677.

[29] Y. Jaccard, J.I. Martin, M.-C. Cyrille, M. Velez, J.L. Vicent, I.K. Schuller, Phys. Rev. B 58, 8232 (1998).

[30] J.I. Martin, M. Velez, A. Hoffmann, I.K. Schuller, .L.Vincent, Phys.Rev.Lett. 83 (1999)1022.

[31] J.I. Martin, M. Velez, A.Hoffmann, I.K. Schuller, J.L. Vincent,Phys.Rev.B 62 (2000) 9110.

[32] A. Hoffmann, P.Prieto, I.K. Schuller, Phys.Rev.B 61 (2000) 6985.

[33] M. Velez, J.I. Martin, J.E. Villegas, A. Hoffmann, E.M. Gonzalez, J.L. Vicent, I.K. Schuller, J. of Magn. and Magn. Mat., 320 (2008) 2547.

[34] J.I. Martin, M. Velez, J. Nogues, and I.K. Schuller, Phys. Rev.Lett. 79, (1997) 1929.

[35] A.E. Ozmetin,, Ph.D. Dissertation, Texas A&M University, College Station, USA. (2009).

[36] C. Reichhardt, J. Groth, C. J. Olson, S. B. Field, F. Nori, Phys.Rev.B 54 (1996) 16108 .

[37] F. Rousseaux, D. Decanini, F. Carcenac, E. Cambril, M. F. Ravet, C.Chappert, N. Bardou, B. Bartenlian, P. Veillet, J. Vac. Sci. Technol. B,13, (1995) 2787.

[38] M. Hehn, K. Ounadjela, J.-P. Bucher, F. Rousseaux, D. Decanini, B. Bartenlian, C. chappert, Science, 272, (1996) 1782.

[39] J.P. Silverman, J.Vac.Sci.Technol.B16 (1998)3137

[40] G. Simon, A. M. Haghiri-Gosnet, J. Bourneix, D. Decanini, Y. Chen, F. Rousseaux, H. Launois, B. Vidal, J. Vac.Sci.Technol.B 15 (1997)2489

[41] D. D. Awschalom, M. A. McCord, and G. Grinstein, Phys. Rev. Lett. 65 (1990) 783.

[42] T.H.P. Chang, D.P. Kern, E. Kratschmer, K.Y. Lee, H.E.Luhn, M.A. McCord, S.A. Rishton ,Y. Vladimirsky, IBM J. Res. Dev. 32 (1988) 462.

[43] G.M. Shedd , P.E. Russell, Nanotechnology 1 (1990) 67.

[44] C.F. Quate, in Scanning Tunneling Microscopy and Related Methods edited by. R.J. Behm, N. Garcia and H. Rohrer, Kluwer Academic Publishers, Dordrecht, (1990).

[45] J. F. Smyth, S. Schultz, D. R. Fredkin, D. P. Kern, S. A. Rishton, H.Schmid, M. Cali, T. R. Koehler, J. Appl. Phys. 69 (1991) 5262.

[46] A. Maeda, M. Kume, T. Ogura, K. Kuroki, T. Yamada, M. Nishikawa, Y. Harada, J. Appl. Phys. 76 (1994) 6667.

[47] K. J. Kirk, J. N. Chapman, and C. D. W. Wilkinson, Appl. Phys. Lett. 71 (1997) 539.

[48] J. I. Martín, Y. Jaccard, A. Hoffmann, J. Nogués, J. M. George, J. L. Vicent, Ivan K. Schuller, J. Appl. Phys. 84 (1998) 411.

[49] J. F. Smyth, S. Schultz, D. R. Fredkin, D. P. Kern, S. A. Rishton, H. Schmid, M. Cali, T. R. Koehler , J. Appl. Phys. 69 (1991) 5262.

[50] Atsushi Maeda, Minoru Kume, Takashi Ogura, Kazuhiko Kuroki, Takashi Yamada, Madoka Nishikawa, Yasoo Harada, J. Appl. Phys. 76

(1994) 6667.

[51] K. J. Kirk, J. N. Chapman, C. D. W. Wilkinson, Appl. Phys. Lett. 71 (1997) 539.

[52] S. Franssila, Introduction to Micro Fabrication, J. Wiley, Chichester,(2004).

[53] L.Reimer, Scanning Electron Microscopy, Springer, Berlin , (1985).

[54] G.Yi, and W.Schwarzacher, Appl.Phys.Lett 74, (1999) 1746.

[55] X.Y. Zhang, and J.Y. Dai, Nanotechnology 15, (2004) 1166.

[56] J..Yao , J.Tang J, D .Wu , D.Sun , K.Xue , B.Ren , B.Mao , Z.Tian , Surface Science,514 (2002), 108.

[57] M.Wong , A.Berenov , X.Qi , M.Kappers , Z.Barber , B.Illy , Z.Lockman , M.Ryan, MacManus-Driscoll JL, Nanotechnology, 14 (2003) 968.

[58] C.A. Ross ,M.Hwang , M.Shima , H.I.Smith , M.Farhoud , T.A.Savas, W.Schwarzacher, J.Parrochon , W.Escoffier , H.N.Bertram , F.B.Humphrey , M.Redjdal , J. of Magn. and Magn.Mat. 249 (2002) 200.

[59] C.A. Ross , S. Haratani , F.J.Castano ,Y. Hao , M.Hwang , M.Shima , J.Y.Cheng , B.Vogeli, Farhoud M, Walsh M, Smith HI, J. of Appl. Phys., 91 (2002) 6848.

[60] M.Shima , M.Hwang , C.A.Ross , J. of Appl. Phys., 93 (2003) 3440.

[61] F. A. Lowenheim, Electroplating, McGraw-Hill, New York, (1978).

[62] G.Binnig,C.F.Quate,C.Gerber, Phys. Rev. Lett.,56 (1986) 930.

[63] G.Binnig, C.Gerber , E. Stolle, T.Albrecht, C.F.Quate, Europhys. Lett. 3 (1987) 1281.

[64] D. Smith , H.Horber, C.Gerber, G.Binnig , Science, 245 (1989) 43.

[65] G. Binnig, H. Rohrer, C. Gerber, E. Weibel , Phys.Rev.Lett.,49 (1982) 57.

[66]Y. Martin , H. K. Wickramasinghe, Appl.Phys.Lett.,50 (1987) 1455.

[67] J. J. Sáenz, N. García, P. Grütter, E. Meyer, H. Heinzelmann, R. Wiesendanger, L. Rosenthaler, H. R. Hidber, and H.-J. Güntherodt, J.Appl.Phys.62 (1987) 4293

[68] A.K. Petford-Long, in Spin Electronics edited by M.Ziese and M.Thornton, Springer, Berlin, (2001).

[69] G. Bochi, H. J. Hug, D. I. Paul, B. Stiefel, A. Moser, I. Parashikov, H.-J. Güntherodt, R. C. O'Handley, Phys.Rev.Lett., 75(1995) 1839

[70] F. Schippan, G. Behme, L. Däweritz, K. H. Ploog, B. Dennis, K.-U. Neumann, K. R. A. Ziebeck, J. Appl. Phys. 88 (2000) 2766

[71] R. D. Gomez, T. V. Luu , A. O. Pak, K. J. Kirk, J. N. Chapman, J. of Appl. Phy. 85 (1999) 6163

[72] A Fernandez, M.R Gibbons, C.J Cerjan, J. of Magn. and Magn. Mat. 190 (1998) 71.

[73] S.Porthun , L. Abelmann , C. Lodder , J. of Magn. and Magn. Mat. 182 (1998) 238.

[74] K.-h. Han, D. Spemann, P. Esquinazi, R. Höhne, V. Riede, T. Butz, Advanced Materials 15 (2003) 1719

[75] S.Landis, B. Rodmacq, B. Dieny, Phys. Rev.B 62 (2000) 12271.

[76] D. Jiles, Introduction to Magnetism and Magnetic Materials, Chapman and Hall, London, (1998).

[77] R. Proksch, D. Dahlberg, in Modern Techniques for Characterizing Magnetic Materials edited by Yimei Zhu, Kluwer Academic Publishers ,Boston , (2005).

[78] L.Abelmann, A. van den Bos, C. Lodder, in Magnetic Microscopy of Nanostructures edited by H. Hopster and H.P. Oepen, Springer, Berlin, (2005).

[79] A. Thiaville, J. Miltat, J.M. Garcia, in Magnetic Microscopy of Nanostructures edited by H. Hopster and H.P. Oepen, Springer, Berlin,(2005).

[80] Z.Ye, H. Liu, Z. Luo, H. Lee,W.Wu, D. Naugle, I Lyuksyutov, Nanotechnology 20 (2009) 045704

[81] A.I. Buzdin, Rev. Mod. Phys., 77 (2005) 935.

[82] V. Vlasko-Vlasov, U. Welp, G. Karapetrov, V. Novosad, D. Rosenmann, M.Iavarone, A. Belkin, W.K. Kwok, Phys. Rev. B., 77 (2008) 134518.

[83] U. Patel, Z. L. Xiao, J. Hua, T. Xu, D. Rosenmann, V. Novosad, J. Pearson, U. Welp, W. K. Kwok, G. W. Crabtree, Phys.Rev.B 76 (2007) 020508.

VITA

Han Gil Lee was born to Yongsoo Lee and Gakhyun Youn in Gwangju, Republic of Korea. He received his B.S. degree in astronomy and M.S degree in physics from Yonsei University, Seoul, Korea. in 1996 and in 1998. After working as a weather forecast officer from 1998 to 2001 in the Korean Air Force, he entered the Department of Physics at Texas A&M University, College Station, TX. in 2002. He received his M.S degree in physics and Ph.D. degree in applied physics from Texas A&M University in 2005 and in 2010.

He may be reached at i21road@hotmail.com. Direct mail can be addressed to : Department of Physics, TAMU 4242, Texas A&M University,College Station, Texas 77843-4242.